Universidade Federal de Pernambuco
Centro de Ciências Exatas e da Natureza
Departamento de Física
Rodrigo Galvão dos Santos

Second-harmonic confocal microscopy of single β–BBO nanocrystals

Recife
2017

Rodrigo Galvão dos Santos

Second-harmonic confocal microscopy of single β–BBO nanocrystals

Dissertação apresentada ao Programa de Pós-Graduação em Física da Universidade Federal de Pernambuco, como requisito parcial para a obtenção do título de Mestre em Física.

Universidade Federal de Pernambuco
Centro de Ciências Exatas e da Natureza
Departamento de Física

Orientador: Leonardo de Souza Menezes
Coorientador: Cid Bartolomeu de Araújo

Recife
2017

Catalogação na fonte
Bibliotecário Jefferson Luiz Alves Nazareno CRB 4-1758

S237s Santos, Rodrigo Galvão dos.
Second-harmonic confocal microscopy of single ß-BBO nanocrystals / Rodrigo Galvão dos Santos – 2017.
54f.: fig.; tab.

Orientador: Leonardo de Souza Menezes.
Dissertação (Mestrado) – Universidade Federal de Pernambuco. CCEN. Física. Recife, 2017.
Inclui referências e apêndice.

1. Óptica. 2. Nano-óptica. 3. Microscopia confocal. I. Menezes, Leonardo de Souza. (Orientador). II. Titulo.

535 CDD (22. ed.) UFPE-FQ 2017-47

Rodrigo Galvão dos Santos

Second-harmonic confocal microscopy of single β–BBO nanocrystals

Dissertação apresentada ao Programa de Pós-Graduação em Física da Universidade Federal de Pernambuco, como requisito parcial para a obtenção do título de Mestre em Física.

Aprovada em: 31/07/2017.

Leonardo de Souza Menezes
Orientador
Universidade Federal de Pernambuco

Cid Bartolomeu de Araújo
Co-Orientador
Universidade Federal de Pernambuco

Edilson Lucena Falcão Filho
Examinador Interno
Universidade Federal de Pernambuco

Adriana Fontes
Examinadora Externa
Universidade Federal de Pernambuco

Recife
2017

RESUMO

Nesta dissertação de mestrado, nós aplicamos a técnica de Microscopia Confocal (MC) para caracterização óptica de nanocristais (NCs) individuais de Beta-Borato de bário (BBO). A MC é capaz de produzir imagens por reflexão e fluorescência com elevada relação sinal-ruído. Nosso aparato experimental permite que a medida da resposta de polarização seja registrada e que os resultados sejam usados para determinar a orientação dos NCs bem como obter informações sobre o tensor de susceptibilidade NL, permitindo uma caracterização detalhada da amostra.NCs de BBO de síntese própria foram previamente caracterizados por diversas técnicas como difração de raio-X (DRX), microscopia eletrônica de transmissão de alta resolução (METAR), difração de elétrons de área selecionada (DEAS) e refletância difusa (RD), garantindo que foi obtida uma fase cristalina única e não centrossimétrica. Os NCs têm um tamanho médio de 150 nm×15 nm×15 nm e essas agulhas são orientadas na direção do eixo cristalográfico c. Por outro lado, a METAR e a DEAS mostraram a presença de defeitos nas agulhas compostos por cristalitos de cerca de 10 nm de diâmetro que são formados durante o crescimento pela rotação dos planos cristalográficos em torno do eixo c. Devido à propriedades simétricas do BBO, a técnica empregada neste trabalho não é capaz de distinguir tais rotações, logo, os defeitos são efetivamente invisíveis à MC assim como às medidas de polarização. O arranjo experimental usa um laser de Ti:Sa (120 fs, 76 MHz, 820 nm) como a fonte luminosa para um microscópio confocal invertido manufaturado, que emprega uma objetiva posicionada num módulo piezo para varredura da amostra com relação à posição focal do laser. Um espelho dicroico atua como um divisor de feixe, garantindo a incidência do laser na amostra e a transmissão do sinal de SH. O aspecto confocal é obtido usando um pinhole de 10 μm no caminho de detecção. Informação espectral é obtida com um monocromador equipado com uma fotomultiplicadora. Uma placa de meia onda colocada antes do espelho dicroico permite medidas do sinal de SH como função da orientação de polarização do laser. Diversas imagens de NCs individuais foram feitas por raster scan da amostra em 2 e 3 dimensões, mostrando uma boa concordância com a teoria de formação de imagens correspondente. A dependência de polarização do sinal de SH permitiu a distinção entre partículas individuais e agregados e os dados foram ajustados com um modelo que leva em consideração as simetrias do BBO e os elementos ópticos do setup. O modelo considera: i) a aproximação eletrostática; ii) os efeitos da objetiva de microscópio usada para focalizar a luz na amostra em configuração de reflexão e iii) as propriedades de $\chi^{(2)}$ para os NCs de β–BBO. Os resultados constituem uma prova de conceito para MC de alta resolução de emissores individuais NL bem como uma caracterização óptica de NCs de BBO até então não descrita na literatura.

Palavras-chave: Microscopia confocal. Beta-borato de bário. Nano-óptica. Geração de segundo harmônico.

ABSTRACT

In this M. Sc. thesis, we apply the Confocal Microscopy (CM) technique for optical characterization of single β–barium-borate (BBO) nanocrystals (NCs). CM can produce images by reflection and fluorescence with high signal-to-noise ratio. Our experimental setup allows the measurement of the SH polarization response to be recorded and the results can be used to determine the NCs orientation as well as to obtain information about the NL susceptibility tensor, allowing a detailed characterization of the sample. Home-synthesized BBO NCs were previously characterized by several techniques such as X-ray diffraction (XRD), High-Resolution Transmission Electronic Microscopy (HRTEM), Selected Area Electron Diffraction (SAED) and Diffuse Reflectance (DR), assuring that non-centrosymmetric and single crystalline phase have been synthesized. The NCs have average dimensions of 150 nm×15 nm×15 nm, and these needles are oriented in the direction of the crystallographic c-axis. On the other hand, the HRTEM and SAED showed the presence of defects in the needles composed of crystallites about 10 nm in size that are formed during the growth by the rotation of crystallographic planes around the c-axis. Due to symmetry properties of BBO, the technique employed in this work cannot discern rotations along the c-axis and thus, the defects are effectively irrelevant to SH CM as well to polarization dependent measurements. The experimental setup uses a mode-locked Ti:Sapphire laser (120 fs, 76 MHz, 820 nm) as a light source for a home-made inverted optical confocal microscope employing a 100X NA=1.25 objective, set under a piezo module for scanning the sample in relation to the laser focal region. A dichroic mirror serves as a beam splitter, ensuring the incidence of the laser on the sample and the transmission of the SH signal. The confocal aspect is obtained by using a 10 μm pinhole in the detection path. Spectral information is obtained with a monochromator equipped with a photomultiplier. A half-wave plate placed right before the dichroic mirror allows measurements of the SH signal as a function of the laser polarization orientation. Several images of single NCs were made by raster scanning of the sample in 2 and 3 dimensions, showing a good agreement with the corresponding imaging theory. The polarization dependence of the SH signal allowed the identification of individual particles from aggregates and the data was fitted using a model that takes into account the BBO symmetries and the optical elements in the setup. The model considers: i) the electrostatic approximation; ii) the effects of the microscope's objective used to focus the light on the sample in epi-geometry configuration and iii) the properties of $\chi^{(2)}$ for the β–BBO NCs. The results constitute a proof of concept for high resolution CM of single NL emitters as well an optical characterization for BBO NCs not hitherto described in the literature.

Keywords: Confocal microscopy. Beta-barium-borate. Nano-optics. Second harmonic generation.

LIST OF ABBREVIATIONS AND ACRONYMS

CM	Confocal Microscopy
BBO	Beta-Barium-Borate
NC	Nanocrystal
PG	Point Group
PSF	Point Spread Function
OU	Optical Unit
CSOM	Confocal Scanning Optical Microscope
FWHM	Full Width at Half Maximum

CONTENTS

1 INTRODUCTION

Confocal microscopy (CM) is a well-known technique for biological applications, since it is able to generate high resolution images of structures as large as a couple micrometers with high signal-to-noise ratio. This gain in resolution is attributed to a spatial filter which allows only the sample's portions in the perifocal region to be detected. It is ideal for studying biological systems such as membranes, tissues and cells (KADOUCH et al., 2017; KYMIONIS et al., 2014; VILLANI et al., 2014; HOOVER; SQUIER, 2013; RAJADHYAKSHA et al., 2017). On the other hand, conventional microscopy (*i.e.*, performed without the spatial filter) can be significantly improved if the imaging process is nonlinear. In order to do so, imaging probes can be used when the structures themselves are not able to generate an appreciable nonlinear signal (THEODOSSIOU et al., 2006; ADUR et al., 2014; LIU et al., 2014; LIU et al., 2015). Optical conversion to the ultraviolet range can also have therapeutic applications, since the DNA absorption of UV light can lead to photodamage and eventually apoptosis (WOLF, 2017).

The so-called second-harmonic radiating imaging probes (SHRIMPs) are of special interest for microscopy because they combine an infrared laser source, which has a greater penetration depth in biological tissues, thus especially promising for *in vivo* applications and a shorter emission wavelength, thus increasing the intrinsic resolution of the apparatus, allowing pinholeless optical sectioning, as shall be discussed in the next chapter (MAZUMDER et al., 2017; WEIGELIN; BAKKER; FRIEDL, 2016; WOLF, 2017). In principle, SHRIMPs can be tuned for a large spectral range because their sizes are much smaller than the coherence length, but for longer wavelengths the multiple harmonics are easier to be detected. Moreover, most SHRIMPs have a good transmittance in the visible and near-infrared, due to the wide band-gap.

SHRIMPs do not suffer the effects of photobleaching neither emission intermittency, due to the second harmonic generation (SHG) nature. SHG is a coherent, lossless and ultrafast process involving only a virtual electron energy transition, typically lasting less than a few femtoseconds (BOYD, 2008; POWERS; HAUS, 2017). Since SHG only occurs in materials without an inversion center, a sharp contrast is formed between the signal coming from non-centrosymmetric crystalline structures and other species. It is also possible that some biological samples that lack inversion symmetry are capable of an appreciable SHG without the use of SHRIMPs.

In terms of wavelength conversion and pump power dependence, SHG is similar to two-photon fluorescence (TPF). On the other hand, the physical nature of SHG and TPF are completely different. TPF is a lossy and incoherent process, leaving some of the excitation energy in the sample, resulting in a gradual loss of emission intensity, so that the emitted photons will have less than twice the energy of the input ones. Photothermal microscopy

can be achieved with TPF because the relaxation process creates a temperature profile around the particle (BIJEESH et al., 2017). Both processes can be expressed considering the dipole approximation as:

$$W_0^{(2\omega)} = \sigma_{2p} I_\omega^2, \tag{1.1}$$

where W_0 is the total power irradiated, σ_{2p} is a two-photon cross-section (in Göppert-Mayer units, where 1 GM=$1 \times 10^{-50}\ cm^4 \frac{s}{\gamma}$ and γ is a photon) and I_ω^2 is the square of the excitation intensity. In Equation 1.1, for SHG in spherical particles, we have: $\sigma_{2p} \propto d^2 r^6$, where d is an effective second-order susceptibility and r is the particle's radius. The sixth-order dependence of the cross-section on the particle size leads to a severe sensitivity problem when the particle is smaller than 100 nm in diameter. At such small sizes, deviations from bulk properties are expected since the material is strongly confined and surface instead of volume effects are dominant (KIM et al., 2013). For spherical $BaTiO_3$ nanocrystals (NCs) smaller than 30 nm in diameter, surface effects start to play a stronger role, so polarization dependence measurements are compromised (KIM et al., 2013).

A variety of NCs of inorganic materials have been tested for SHG as well for biological compatibility, including: ZnO (CHAN et al., 2006; GEREN et al., 2009; DANTEC et al., 2011; URBAN et al., 2011), $LiNbO_3$ (GRANGE et al., 2009; DUTTO et al., 2011), $KNbO_3$ (DUTTO et al., 2011; NAKAYAMA et al., 2007; WANG et al., 2012), $NaNbO_3$ (XIAO et al., 2015), $KTiOPO_4$ (LOC et al., 2008; WNUK et al., 2009), $BaTiO_3$ (DANTEC et al., 2011; RODRIGUEZ et al., 2009; HSIEH et al., 2009; HSIEH et al., 2010a) and for this M. Sc thesis, β-BaB_2O_4 (BBO). Among those crystals, the so called polar possess a unique axis of rotation. Crystals of this sort can show a change in permanent dipole with temperature (pyroelectric effect) (BOYD, 2008). Group theory arguments demonstrate that all polar crystal classes are noncentrosymmetric, but not all noncentrosymmetric crystal classes are polar (NYE, 1985). Figure 1 shows how the noncentrosymmetric point groups (PG) can be classified according to the polar character[1]. More about that will be presented in Chapter 2.

Polar crystals naturally lack of inversion center due to the spontaneous polarization. Therefore, they are excellent candidates for nonlinear optical processes (DENEV et al., 2011). Moreover, that feature can be explored to engineer the nonlinear susceptibility (BELLINI et al., 2014). Following the aforementioned classification, BBO fits in the polar category, since it belongs to the 3m PG. The polar character of NCs can be observed by polarization dependent measurements. A common technique for nonlinear imaging microscopy allows to determine the NCs' orientation with respect to the laboratory frame. This is possible because in a multiple-domain NCs, or a cluster of many single-domain NCs with random crystal orientations, depolarization takes place due to the random orientations (PU; PSALTIS, 2016).

[1] Following Hermann–Mauguin notation, rotation axes are denoted by an integer number n. The rotoinversion axes are represented by the corresponding number with a macron, $\overline{n}$. The symbol for a mirror plane (rotoinversion axis $\overline{2}$) is m (HAHN, 2005).

Figure 1 – 21 Noncentrosymmetric PGs. On the left the non-polar (11 PGs) and on the right the polar (10 PGs).

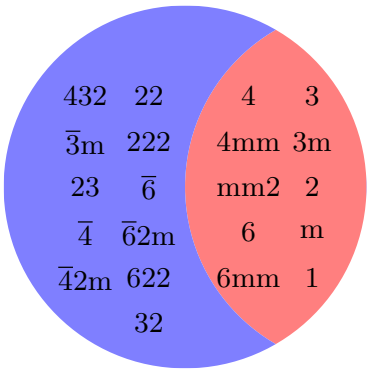

SHG microscopy is a less invasive and destructive technique for characterizing nanomaterials when compared to other techniques like transmission electron microscopy (TEM). Although the latter has a better spatial resolution than the former, polarization dependent SHG can be used for investigations of the nonlinear optical properties associated to different crystal symmetries.

In this work, the relative orientations of BBO NCs were determined by SHG, thus confirming the crystallographic lattice and shape of second-order susceptibility tensor, $\chi^{(2)}$. The final image obtained by SHRIMPs is limited in resolution by the Point Spread Function (PSF) of the nonlinear imaging process, typically ≈200 nm for SHG in CM.

1.1 Thesis objectives

The main aim of this research was the construction of a home-made inverted microscope for SH confocal microscopy of single BBO NCs. The confocal scanning optical microscope must be able to perform raster scans, record SH spectra and the polarization response for single emitters, so the apparatus can be used to study SHG in individual NCs. The results are then compared to the pertinent imaging and SHG theories.

1.2 Thesis outline

This M. Sc. thesis is composed of four chapters. Chapter 1 was a brief introduction, Chapter 2 introduces the principles of CM for studying single BBO nanocrystals as well the imaging process based on SHG. Chapter 3 presents the experimental setup, the methodology and the results obtained. Finally, in Chapter 4 the main results are summarized and perspectives for future works are given.

2 BACKGROUND AND MOTIVATION

2.1 Basics of Second-Order Nonlinear Optics

This section presents some considerations about the origins of second harmonic (SH) in condensed matter. We derive the polarization density in 2ω excited by an optical field of frequency ω following the anharmonic oscillator model, and show that it is composed of three components: nonlinear, DC and linear. The model also describes the overall behavior of the nonlinear susceptibility $\chi_{NL}^{(2\omega)}$, which is real and frequency independent for lossless media in the low frequency range. Special attention is given to β–BBO nanocrystals, which is the system of interest for this M. Sc. thesis. Considering symmetry properties of the crystalline lattice, we show that the shape of $d_{ij}^{(2\omega)}$ for that crystal class and construct the polarization response for a single SH emitter. Furthermore, we apply to the model two corrections introduced by the high numerical aperture objective used in the system. First, we correct the polarization response taking into account the axial polarization component introduced by the tight focusing conditions and then we show the effect of the collection efficiency.

2.1.1 On the physical origins of Nonlinear Optics

The first observation of optical harmonics was reported by Franken *et al.* in 1961 (FRANKEN et al., 1961). In that experiment, a ruby laser operating at 694.3 nm was focused in a sample of crystalline quartz and emergent radiation with twice the fundamental frequency was detected. The conversion efficiency was $\approx 10^{-8}$. Following that experiment, more efficient systems and materials allowed observation of yields closer to unit.

The optical properties of nonlinear materials are described by expanding the polarization in a power series of the incident electrical field as:

$$\mathbf{P}(t) = \epsilon_0 \left[\chi^{(1)} \mathbf{E}(t) + \chi^{(2)} \mathbf{E^2}(t) + \chi^{(3)} \mathbf{E^3}(t) + \ldots \right], \tag{2.1}$$

where $\mathbf{P}(t)$ is the polarization density (dipole moment per unit volume), $\mathbf{E}(t)$ is the incident electrical field, the coefficients $\chi^{(n)}$ are the n-th-order susceptibilities of the medium and ϵ_0 is the vacuum permittivity. From equation 2.1, we see that even order harmonics are only seen in non-centrosymmetric materials. The reason for that is straightforward: since the inversion operation is symmetric, the relation between $\mathbf{P}$ and $\mathbf{E}$ needs to remain unchanged after the inversion, thus $\chi^{(even)} = 0$.

A simple way to understand the physical origins of NO is solving the 1-D oscillator in a non harmonic potential, analogous to the movement of a bound electron in a crystal lattice, for instance:

$$V_T = V_0(x) + \delta V(x) = \frac{m\omega_0 x^2}{2} + \frac{m\beta x^3}{3}, \tag{2.2}$$

where V_T is a potential composed of a harmonic part ($V_0(x)$) and $\delta V(x)$ is a non harmonic perturbation. ω_0 is the fundamental oscillator frequency and β determines the anharmonic perturbation amplitude. Suppose that an external field excites the system having the form:

$$E(t) = \frac{1}{2}\left[E_0\left(e^{i\omega t} + e^{-i\omega t}\right)\right] = E_0 \cos \omega t \tag{2.3}$$

The equation of motion will be:

$$\ddot{x} + \gamma\dot{x} + \omega_0^2 x + \beta x^2 = \frac{qE_0}{2m}\left(e^{i\omega t} + e^{-i\omega t}\right), \tag{2.4}$$

where x is the displacement from the potential minimum; q and m are the electron's fundamental charge and mass respectively; $m\beta x^2$ is the anharmonic restoring force corresponding to $\frac{m\beta x^3}{3}$ and γ is a damping constant. We look for the polarization at 2ω, so assuming a solution like:

$$x = \frac{1}{2}\left(q_1 e^{i\omega t} + q_2 e^{2i\omega t} + c.c.\right) \tag{2.5}$$

Solving equation of motion at the first order of the parameter β we get:

$$q_1 = \left(\frac{qE_0}{m}\right)\frac{1}{(\omega_0^2 - \omega^2) + i\omega\gamma} \tag{2.6}$$

$$q_2 = \left(\frac{qE_0}{m}\right)^2 \frac{-\beta}{2\left[(\omega_0^2 - \omega^2) + i\omega\gamma\right]^2 (\omega_0^2 - 4\omega^2 + 2i\omega\gamma)} \tag{2.7}$$

The linear and nonlinear susceptibilities are given by:

$$P^{\omega}(t) = \frac{\epsilon_0}{2}\left(\chi_L^{(\omega)} E_0 e^{i\omega t} + c.c.\right) = \frac{Nq}{2}\left(q_1 e^{i\omega t} + c.c.\right) \tag{2.8}$$

$$P^{2\omega}(t) = \frac{\epsilon_0}{2}\left(\chi_{NL}^{(2\omega)} E_0^2 e^{2i\omega t} + c.c.\right) = \frac{Nq}{2}\left(q_2 e^{2i\omega t} + c.c.\right), \tag{2.9}$$

where N is the number of dipoles excited. Thus:

$$\chi_L^{(\omega)} = \frac{Nq^2}{m\epsilon_0\left[(\omega_0^2 - \omega^2) + i\omega\gamma\right]} \tag{2.10}$$

$$\chi_{NL}^{(2\omega)} = \frac{-\beta N q^3}{2m^2\epsilon_0\left[(\omega_0^2 - \omega^2) + i\omega\gamma\right]^2 (\omega_0^2 - 4\omega^2 + 2i\omega\gamma)} \tag{2.11}$$

We notice that the parameter β is zero for centrosymmetric materials, since it is the origin of the non harmonic perturbation, so the second harmonic is not observed in such materials (YARIV, 1989). One way to obtain a noncentrosymmetric potential is to add or remove a charge in any point of a lattice of a unit cell in a centrosymmetric crystal. In Figure 2 we see that the polarization wave has components with frequencies at the original frequency and at the double of the original frequency, plus a DC component. We also notice an important property of the nonlinear susceptibilities for lossless media ($\gamma = 0$), the fact that its components are real. In the next section some other properties of the nonlinear susceptibilities will be discussed as well the role of the lattice symmetry on the presence of null elements.

Figure 2 – Solution for the 1-D oscillator in a non harmonic potential. (a) Nonlinear polarization wave (thick line). The thin, dotted and dashed lines correspond, respectively, to nonlinear, DC and linear components; (b) aspect of $\chi_{NL}^{(2\omega)}$ for a lossless medium at the low frequency range. Solid line is $Re\left[\chi_{NL}^{(2\omega)}\right]$ and dashed line is $Im\left[\chi_{NL}^{(2\omega)}\right]$.

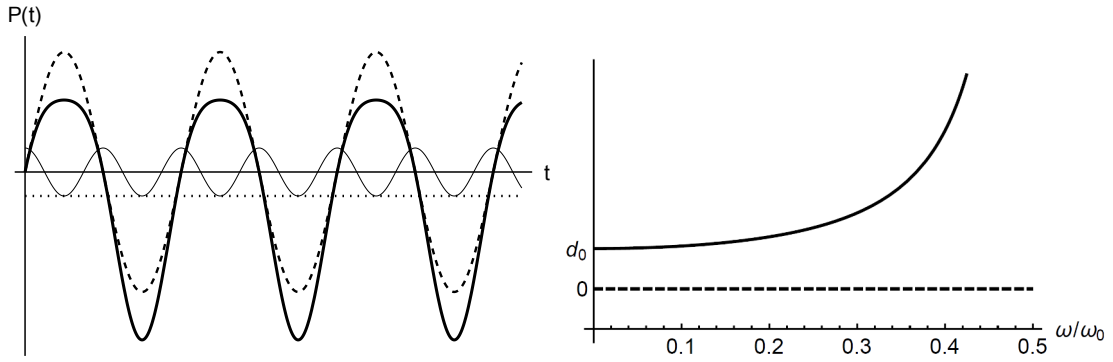

(a) (b)

2.1.2 Properties of the nonlinear susceptibilities

The complete description of the interaction between three waves in a nonlinear medium requires that we determine several components of the nonlinear susceptibility tensors, so it is useful to apply some properties in order to reduce the number of independent variables. The properties can be constructed for the second-order susceptibility $\chi^{(2)}$, but can easily be extended for the higher-order susceptibilities (BOYD, 2008). Writing the nonlinear polarization as (ϵ_0 is embedded in the susceptibility for simplicity):

$$P_i\left(\omega_n+\omega_m\right)=\sum_{jk}\sum_{(nm)}\chi_{ijk}^{(2)}\left(\omega_n+\omega_m;\omega_n,\omega_m\right)E_j\left(\omega_n\right)E_k\left(\omega_m\right), \tag{2.12}$$

We can take the following theorems into account:

Theorem 2.1 (Physical fields are real)**.**

$$\chi_{ijk}^{(2)}\left(\omega_n+\omega_m;\omega_n,\omega_m\right)^*=\chi_{ijk}^{(2)}\left(-\omega_n-\omega_m;-\omega_n,-\omega_m\right) \tag{2.13}$$

Proof. Since the fields and polarization are real quantities related to each other through the second-order susceptibility, their complex amplitude must obey the relation: $E^*\left(\omega\right)=E\left(-\omega\right)$, therefore the positive- and negative-frequency components of the susceptibility must be related in that manner. ■

Theorem 2.2 (Permutation symmetry)**.**

$$\chi_{ijk}^{(2)}\left(\omega_n+\omega_m;\omega_n,\omega_m\right)=\chi_{ikj}^{(2)}\left(\omega_n+\omega_m;\omega_m,\omega_n\right) \tag{2.14}$$

Proof. The nonlinear susceptibility is unchanged by the simultaneous interchange of its last two frequency arguments and its last two Cartesian indices. Another way to prove

that is making one of the frequency arguments equal to zero and double the value of the other, preserving the result. It cannot matter which is the first field and which is the second field in products such as $E_j(\omega_n) E_k(\omega_m)$. ■

Theorem 2.3 ($\chi^{(2)}$ is real for lossless medium)**.** *For a lossless medium all of the components of* $\chi^{(2)}_{ijk}(\omega_n + \omega_m; \omega_n, \omega_m)$ *are real.*

Proof. This result can be seen from equation 2.11 in the limit when the applied frequency is significantly different from the resonance frequency. The general proof that $\chi^{(2)}_{ijk}$ is real for a lossless medium is verified by the quantum mechanical equation of $\chi^{(2)}_{ijk}$ in the same limit. ■

Theorem 2.4 (Full permutation symmetry for a lossless medium)**.** *For a lossless medium all of the frequency arguments of* $\chi^{(2)}_{ijk}(\omega_n + \omega_m; \omega_n, \omega_m)$ *are interchangeable as long as the corresponding Cartesian indices are interchanged simultaneously.*

Proof. Full permutation symmetry can be deduced from the field energy density within a nonlinear medium:

$$\begin{aligned} U = & \frac{1}{2} \sum_{ij} \sum_{n} \chi^{(1)}_{ijk}(\omega_n) E^*_i(\omega_n) E_j(\omega_n) \\ & + \frac{1}{3} \sum_{ijk} \sum_{n} \chi^{(2)'}_{ijk}(-\omega_n - \omega_m; \omega_m, \omega_n) E^*_i(\omega_m + \omega_n) E_j(\omega_m) E_k(\omega_n) \\ & + \cdots, \end{aligned} \tag{2.15}$$

where $\chi^{(2)'}_{ijk}$ is a coefficient in the power series expansion of U, related to the nonlinear susceptibility. Since the order in which the fields are multiplied is immaterial, the quantity $\chi^{(2)'}_{ijk}$ possesses full permutation symmetry. This demonstration is only valid for the lossless case, because the internal energy is a function of state. ■

Theorem 2.5 (Kleinman's Symmetry)**.** *In the low frequency range for lossless medium the susceptibilities are essentially independent of frequency.*

Proof. This result can be seen from equation 2.11 in the limit when the applied frequency is significantly smaller than the resonance frequency. In the low frequency range, the system responds essentially instantaneously to the applied field and the nonlinear polarization can be expressed in the time domain by the relation:

$$\tilde{P}(t) = \chi^{(2)} \tilde{E}(t)^2, \tag{2.16}$$

where $\chi^{(2)}$ can be taken to be a constant. The condition of full permutation is also valid, so we can permute the indices of the susceptibility without permuting the frequencies, so:

$$\begin{aligned} \chi^{(2)}_{ijk}(\omega_3 = \omega_1 + \omega_2) &= \chi^{(2)}_{jki}(\omega_3 = \omega_1 + \omega_2) = \chi^{(2)}_{kij}(\omega_3 = \omega_1 + \omega_2) \\ &= \chi^{(2)}_{ikj}(\omega_3 = \omega_1 + \omega_2) = \chi^{(2)}_{jik}(\omega_3 = \omega_1 + \omega_2) \\ &= \chi^{(2)}_{kji}(\omega_3 = \omega_1 + \omega_2) \end{aligned} \tag{2.17}$$

This result is valid whenever the dispersion of the susceptibility can be neglected. ■

Theorem 2.6 (Neumann's principle)**.** *If a crystal is invariant with respect to certain symmetry operations, its physical properties must also be invariant with respect to the same symmetry operations.*

Proof. The proof is straightforward. Since nonlinear susceptibilities are tensors, transformations that do not change the physical reference between the fields and the media leave the susceptibilities invariant. Therefore, measurements made in symmetry-related directions will give the same result (NEWNHAM, 2005). For instance, considering the inversion:

$$T_{i'i} = (-1)\,\delta_{i'i} \tag{2.18}$$

on a medium invariant under inversion, the susceptibility tensor of the inverted medium is:

$$\chi^{(2)}_{i'j'k'} = (-1)^3\,\chi^{(2)}_{ijk} = -\chi^{(2)}_{ijk} = \chi^{(2)}_{ijk} = 0, \tag{2.19}$$

as expected, for a medium invariant under inversion cannot generate SH. On the other hand, the reverse is not true, since the symmetry of a physical property can be higher than that of the point group. ■

Definition 2.1 (Contracted notation)**.** *When Kleinman symmetry is valid, it is useful to introduce the tensor:*

$$d_{ijk} = \frac{1}{2}\chi^{(2)}_{ijk} \tag{2.20}$$

The nonlinear polarization can be written as:

$$P_i\left(\omega_n + \omega_m\right) = \sum_{jk}\sum_{(nm)} 2d_{ijk}E_j\left(\omega_n\right)E_k\left(\omega_m\right) \tag{2.21}$$

Assuming that d_{ijk} is symmetric in its last two indices (valid for second harmonic generation and when Kleinman symmetry is valid), we have:

$$d_{ijk} = d_{ikj} \equiv d_{il} = \begin{bmatrix} d_{11} & d_{12} & d_{13} & d_{14} & d_{15} & d_{16} \\ d_{21} & d_{22} & d_{23} & d_{24} & d_{25} & d_{26} \\ d_{31} & d_{32} & d_{33} & d_{34} & d_{35} & d_{36} \end{bmatrix} \tag{2.22}$$

Therefore we simplified the number of components of the tensor from 27 to 18. We could go even further by a permutation of all indices, so d_{il} would have 10 independent elements. We can describe the nonlinear polarization leading to second-harmonic generation by the matrix equation:

$$\begin{bmatrix} P_x\left(2\omega\right) \\ P_y\left(2\omega\right) \\ P_z\left(2\omega\right) \end{bmatrix} = 2\begin{bmatrix} d_{11} & d_{12} & d_{13} & d_{14} & d_{15} & d_{16} \\ d_{21} & d_{22} & d_{23} & d_{24} & d_{25} & d_{26} \\ d_{31} & d_{32} & d_{33} & d_{34} & d_{35} & d_{36} \end{bmatrix}\begin{bmatrix} E_x\left(\omega\right)^2 \\ E_y\left(\omega\right)^2 \\ E_z\left(\omega\right)^2 \\ 2E_y\left(\omega\right)E_z\left(\omega\right) \\ 2E_x\left(\omega\right)E_z\left(\omega\right) \\ 2E_x\left(\omega\right)E_y\left(\omega\right) \end{bmatrix} \tag{2.23}$$

The linear and nonlinear susceptibilities for any particular crystal are determined by all the symmetry properties. According to the group theory, the crystals can be classified as belonging to one of 32 possible classes depending on the point group symmetry of the crystal. 11 of those classes possess inversion symmetry, remaining 21 non-centrosymmetric. Figure 3 shows some of the Bravais lattices, followed by the respective packing factors (KITTEL, 1986).

Figure 3 – Some Bravais lattices. The atoms are represented as half the size of the packing factor for comparison. (a) Simple Clubic (SC); (b) Body Centered Cubic (BCC); (c) Face Centered Cubic (FCC); (d) Diamond Lattice (DL).

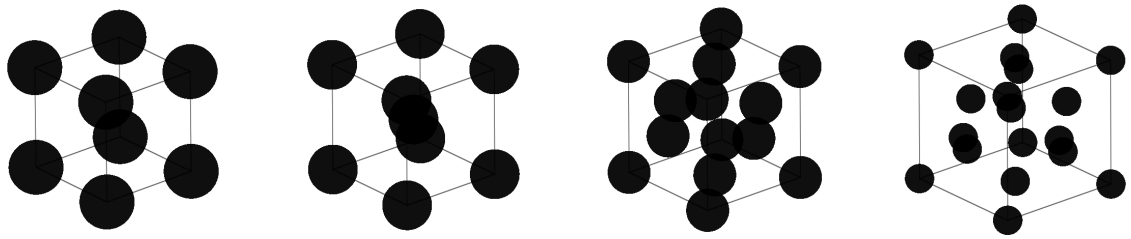

(a) (b) (c) (d)

Definition 2.2 (Packing factors)**.** *Considering Figure 3 above, the packing factor (PF) is:*

$$PF = \frac{N \cdot V_a}{V_c}, \tag{2.24}$$

where N is the number of atoms in the unit cell, V_a is the volume occupied by those atoms and V_c is the volume of the unit cell.

For the SC lattice, the largest atomic radius possible is $R = \frac{a}{2}$, thus the PF is:

$$PF = \frac{\frac{8}{8}\frac{4\pi}{3}\left(\frac{a}{2}\right)^3}{a^3} = \frac{\pi}{6} \approx 0.524 \tag{2.25}$$

For the BCC lattice, the largest atomic radius possible is given by Pythagoras' theorem applied to the cube's diagonal. We can accommodate only four times the value of R, so that $R = \frac{a\sqrt{3}}{4}$ and thus:

$$PF = \frac{\left(\frac{8}{8}+1\right)\frac{4\pi}{3}\left(\frac{a\sqrt{3}}{4}\right)^3}{a^3} = \frac{\pi\sqrt{3}}{8} \approx 0.680 \tag{2.26}$$

For the FCC lattice, the largest atomic radius possible is given by Pythagoras' theorem applied to the face of the cube. We can accommodate only four times the value of R, so that $R = \frac{a\sqrt{2}}{4}$ and thus:

$$PF = \frac{\left(\frac{8}{8}+\frac{6}{2}\right)\frac{4\pi}{3}\left(\frac{a\sqrt{2}}{4}\right)^3}{a^3} = \frac{\pi\sqrt{2}}{6} \approx 0.740 \tag{2.27}$$

For the diamond structure we have a FCC lattice plus four additional atoms at the coordinates: $\left(\frac{3a}{4}, \frac{a}{4}, \frac{a}{4}\right)$, $\left(\frac{a}{4}, \frac{a}{4}, \frac{3a}{4}\right)$, $\left(\frac{a}{4}, \frac{3a}{4}, \frac{a}{4}\right)$ and $\left(\frac{3a}{4}, \frac{3a}{4}, \frac{3a}{4}\right)$. Applying the Pythagoras' theorem for the distance between two of those extra atoms and its neighbor at one corner of the cube, we get: $d = \frac{a\sqrt{3}}{4}$. We can accommodate only twice the value of R, so that $R = \frac{a\sqrt{3}}{8}$ and thus:

$$PF = \frac{\left(\frac{8}{8} + \frac{6}{2} + 4\right) \frac{4\pi}{3} \left(\frac{a\sqrt{3}}{8}\right)^3}{a^3} = \frac{\pi\sqrt{3}}{16} \approx 0.340, \tag{2.28}$$

which is the less dense of those cubic lattices. For all of those four Bravais lattices, only odd-order harmonics can be generated, since they are all centrosymmetric.

Definition 2.3 (Density of a crystallographic phase)**.** *Taking the cobalt atom as an example, it can form two crystallographic phases: (i) α–Co which is Hexagonal Close Packed (HCP) with a=0.251 nm and c=0.457 nm (Figure 4); (ii) β–Co which is FCC with a=0.355 nm.*

Figure 4 – HCP lattice of α–Co

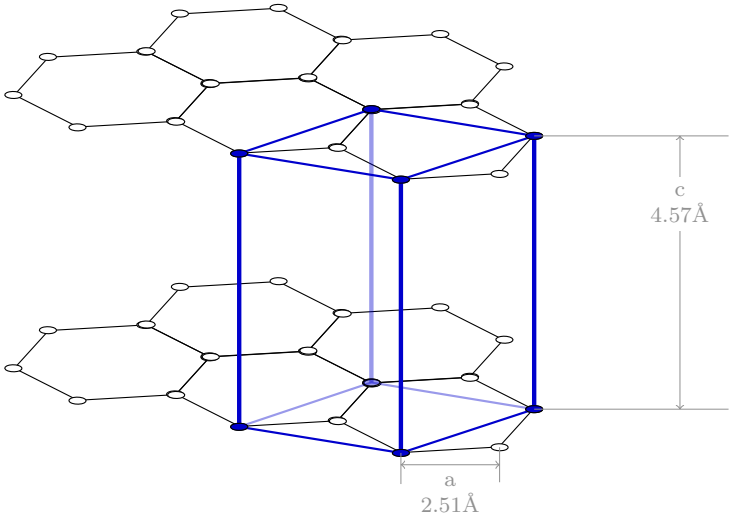

The density of those phases is given by:

$$d = \frac{N \cdot M_a}{V_c \cdot N_a}, \tag{2.29}$$

where N is the number of atoms in each cell, M_a is the atomic weight of Co, V_c is the volume of the cell and N_a is the Avogadro's number. For the FCC lattice (4 atoms in each cell):

$$V_c = a^3 \Rightarrow d = 8749.72 \ Kg \cdot m^{-3} \tag{2.30}$$

For the HCP lattice (6 atoms in each cell):

$$V_c = \frac{3 \cdot c \cdot a^2\sqrt{3}}{2} \Rightarrow d = 8814.08 \ Kg \cdot m^{-3} \tag{2.31}$$

By considering the type of symmetry present in mineral species, they can be categorized as a member of one of seven crystal systems and one of thirty two crystal classes. The symmetries of a crystal can be associated to translational operations or point operations. Translational operations describe patterns across a volume, while point operations describe reflections, rotations and inversions around a point. The crystal systems are useful to determine the optical properties of a sample, since the forms of $\chi^{(1)}$ and $\chi^{(2)}$ are available for all the systems and point groups (PG).

Table 1 – Form of $\chi^{(1)}$ for the seven crystal systems

System	$\chi^{(1)}$
Triclinic	$\begin{bmatrix} xx & xy & xz \\ yx & yy & yz \\ zx & zy & zz \end{bmatrix}$
Monoclinic	$\begin{bmatrix} xx & 0 & xz \\ 0 & yy & 0 \\ zx & 0 & zz \end{bmatrix}$
Orthorhombic	$\begin{bmatrix} xx & 0 & 0 \\ 0 & yy & 0 \\ 0 & 0 & zz \end{bmatrix}$
Tetragonal Trigonal Hexagonal	$\begin{bmatrix} xx & 0 & 0 \\ 0 & xx & 0 \\ 0 & 0 & zz \end{bmatrix}$
Cubic & Isotropic	$\begin{bmatrix} xx & 0 & 0 \\ 0 & xx & 0 \\ 0 & 0 & xx \end{bmatrix}$

Table 1 shows the form of $\chi^{(1)}$ for the seven crystal systems plus the isotropic medium. The cubic is the only isotropic system because $\chi^{(1)}$ is diagonal and with equal components. The form of $\chi^{(2)}$ has been determined for each of the 32 crystal classes, graphically represented in Figure 5 (ZERNIKE; MIDWINTER, 1973).

Figure 5 – Form of the d_{il} matrix. Small dot: zero coefficient; large dot: nonzero coefficient; square: coefficient that is zero when Kleinman's symmetry condition is valid; connected symbols: numerically equal coefficients, but the open-symbol coefficient is oposed in sign to the closed symbol to which it is joined. Dashed connections are valid only under Kleinman's symmetry conditions.

2.1.3 SHG under tight focusing conditions

Beta Barium Borate, β–BaB_2O_4 (BBO), is a trigonal PG 3m (Figure 6), nonlinear optical material transparent from ≈190–3300 nm. Due to the crystal symmetry, the SHG response is determined only by the orientation of the c-axis of the crystal. Historically, BBO has been misplaced at the PG 3, instead of the 3m, leading to imprecise symmetry operations. On the other hand, by looking at Figure 6, both PGs share a similar overall form, and when the elements of the d_{il} matrix are defined accordingly, the misplaced PG 3 can reproduce the results of the PG 3m.

Figure 6 – BBO structure and PG. The ▲–shaped symbol represents the threefold rotation axis. The figure shows how an arbitrary point is symmetrically related to other two (for PG 3) or five (for PG 3m).

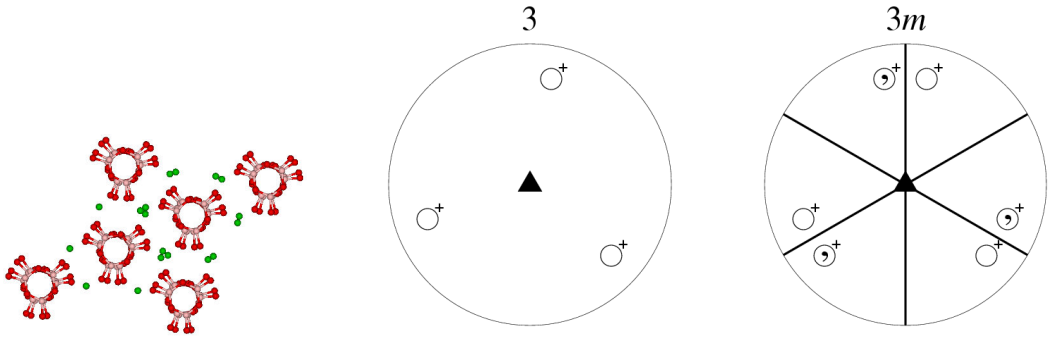

(a) BBO viewed along the c axis

(b) PG 3

(c) PG 3m

For the analysis of this M. Sc. thesis, it is necessary to define the orientation of the crystals with respect to the microscope's objective that will be used in the experiments. For uniaxial crystals, only two angles are required to define the c-axis position, as shown in Figure 7. It is clear from this geometry that the crystals will be symmetric by the operation $\theta_0 \rightarrow \theta_0 \pm \pi$, as well as by any rotation along the c-axis.

In Figure 7, Ω is the collection angle, determined by the numerical aperture (NA) of the objective and γ gives the relative orientation of the polarization in ω. Following the methodology described by (HSIEH et al., 2010a; SCHMIDT et al., 2016), the electric field at the fundamental frequency is decomposed into three orthogonal components in the crystal frame:

$$\mathbf{E}_{\mathbf{p}}^{\omega} = E_{CX}\hat{e}_{CX} + E_{CY}\hat{e}_{CY} + E_{CZ}\hat{e}_{CZ}, \tag{2.32}$$

where X, Y and Z are in the lab frame and $\hat{e}_{CX}$, $\hat{e}_{CY}$ and $\hat{e}_{CZ}$ are in the crystal frame. Applying a proper rotation matrix given by Equation 2.33 and assuming the electrostatic approximation[1] $W_0 \propto |P^{2\omega}|^2$, we get a handy polarization profile chart for the BBO

[1] In the electrostatic approximation, the SHG polarizations can be regarded as three orthogonal SHG dipoles.

Figure 7 – Schematic diagram for a unaxial particle oriented at an arbitrary direction under a LP plane-wave excitation (HSIEH et al., 2010b).

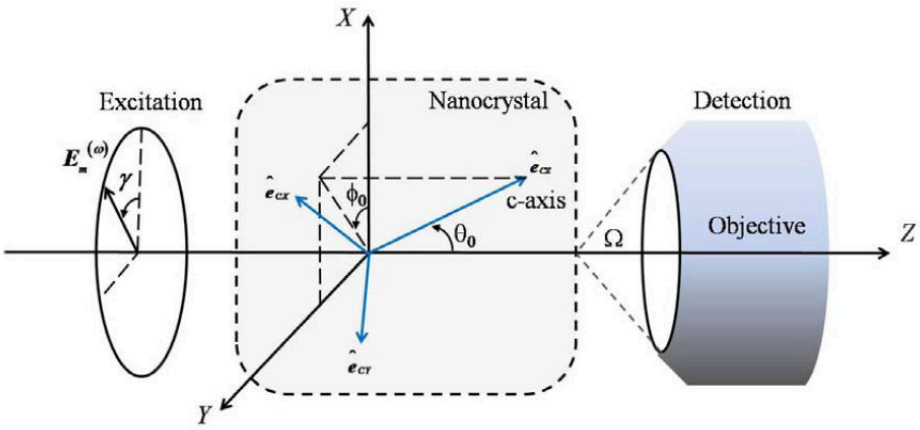

crystals, as shown in Figure 8.

$$R = Rot_Z(\phi_0)Rot_Z(\theta_0) = \begin{bmatrix} \cos\phi_0\cos\theta_0 & -\sin\phi_0 & \cos\phi_0\sin\theta_0 \\ \sin\phi_0\cos\theta_0 & \cos\phi_0 & \sin\phi_0\sin\theta_0 \\ -\sin\theta_0 & 0 & \cos\theta_0 \end{bmatrix} \tag{2.33}$$

The inverse transformation is given by $R^{\top}$. A similar matrix can be deduced for three Euler angles, when rotations along the c-axis are relevant (DOW et al., 2016).

Figure 8 – Theoretical model for the polarization-resolved microscopy for 36 BBO nanocrystals. In this simulation, θ_0 goes from 0 to $\frac{\pi}{2}$ along the columns of the matrix and ϕ_0 goes from 0 to π along the rows of the matrix. d_{22} is taken as 2.0 pm/V (ECKARDT; BYER, 1991; BACHE et al., 2013). (a) all components, (b) only X and Z components (c) only Y and Z components

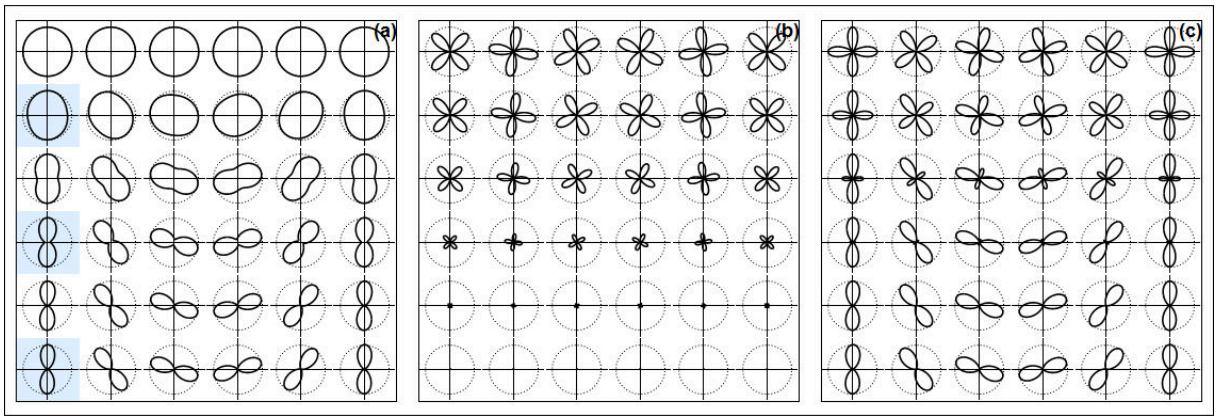

As shown in Figure 8, the polarization response for large θ_0 consists entirely on the Y and Z-components. Moreover, the hourglass shaped curve is unique for a given pair of angles $\{\theta_0, \phi_0\}$. Since low values of θ_0 are less likely to happen due to the crystal's geometry, the uniqueness of the polarization response is sufficient to identify a single emitter, since

a circular pattern would suggest a cluster formation. On the other hand, the incident beam is diffraction limited and linearly polarized, but under intense field confinement at the focus, the focal spot becomes more and more elliptical. Whereas in the paraxial limit the spot is perfectly circular, a strongly focused beam has a spot that is elongated in the direction of polarization, thus introducing a depolarization effect (NOVOTNY; HECHT, 2012). Therefore, the previous approach needs to be corrected by the effects of the depolarization introduced by the high NA objective.

Assuming that **E** is entirely polarized along the x-axis and the incident beam is sufficiently large in diameter, the focused field at the beam waist can be written as (RICHARDS; WOLF, 1959):

$$\begin{aligned} E_X(r,\phi) &= -i\left[f_0(r) + f_2(r)\cos(2\phi)\right] \\ E_Y(r,\phi) &= -if_2(r)\sin(2\phi) \\ E_Z(r,\phi) &= -2f_1(r)\sin(\phi), \end{aligned} \tag{2.34}$$

where:

$$\begin{aligned} f_0(r) &= \int_0^{\Omega} \sqrt{\cos\theta}\sin\theta\,(1+\cos\theta)\,J_0(kr\sin\theta)\,d\theta \\ f_1(r) &= \int_0^{\Omega} \sqrt{\cos\theta}\sin^2\theta J_1(kr\sin\theta)\,d\theta \\ f_2(r) &= \int_0^{\Omega} \sqrt{\cos\theta}\sin\theta\,(1-\cos\theta)\,J_2(kr\sin\theta)\,d\theta \end{aligned} \tag{2.35}$$

θ and ϕ are regular polar coordinates and J_n are Bessel functions of the first kind.

According to those equations, the maximum relative values are: $\frac{|E_Y|^2}{|E_X|^2} = 0.005$ and $\frac{|E_Z|^2}{|E_X|^2} = 0.169$, for a NA=1.25 and λ=820 nm. The aspect of the XYZ components of the original Gaussian field are shown in Figure 9. The figure shows that the Y–component is negligible, but the tight focusing conditions introduce an appreciable Z–component in the incident electrical field. Re-normalizing that contribution, we find that ≈14% of the pump intensity is transfered to the Z–component.

Applying the results of Figure 9 to the ones shown in Figure 8, we get what is shown in Figure 10. Due to the tensorial nature of $\chi^{(2)}$, the depolarization effect mixes all the components together, specially for the introduced Z-component. As a result, some orientations may produce a higher signal when compared to the previous situation. On the other hand, these calculations do not take into account the particles' shape. As it will be shown in the next chapter, the BBO crystals are shaped like needles, so one component is much larger than the others. Therefore, it is expected that the particles behave closer to the represented in Figure 8, since there is a much smaller amount of matter (and therefore electrical dipoles) in the Z-direction, so the depolarization contribution will be even smaller when compared to the main polarization component. That would not be true, however, for spherical particles.

Figure 9 – Magnitudes of the individual field components $|E_X|^2$,$|E_Y|^2$ and $|E_Z|^2$ respectively in the focal plane (z=0).The pixel size is 50 nm and the size of the images is 4x4 μm^2. (b) and (c) are rescaled by a factor of 200X and 6X respectively for comparison.

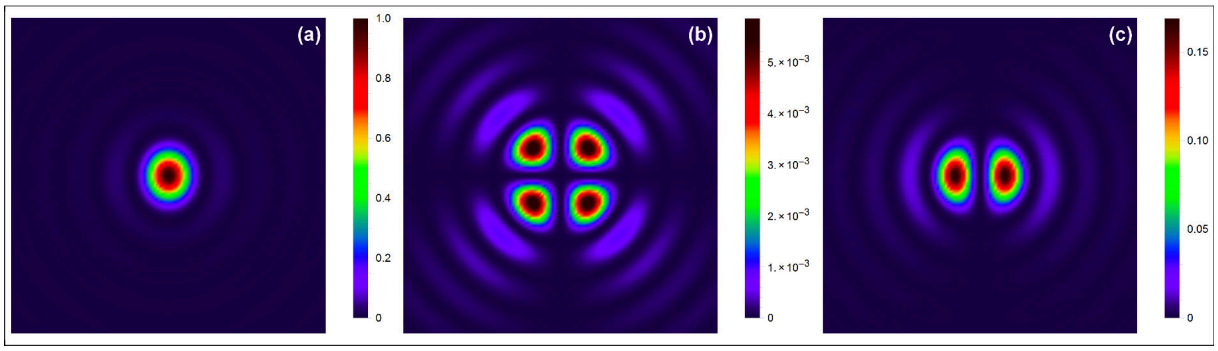

Figure 10 – Same as Figure: 8 but taking into account the effects of the tight focalization

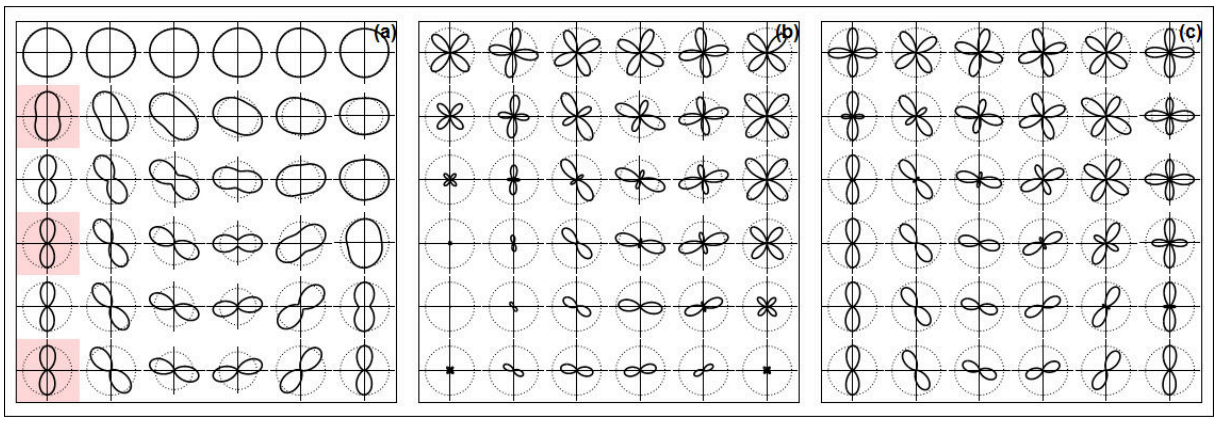

The blue and red plots shown in Figures 8 and 10 will be used to illustrate a last correction that can be done to the theoretical calculations, the effect of the objective's efficiency collection, given by:

$$\eta = \frac{\int_0^{\Omega}\int_0^{2\pi}\left|\mathbf{E}^{(\mathbf{2}\omega)}\right|^2 \sin\theta d\phi d\theta}{\int_0^{\pi}\int_0^{2\pi}\left|\mathbf{E}^{(\mathbf{2}\omega)}\right|^2 \sin\theta d\phi d\theta} \tag{2.36}$$

We notice after performing the integral that η is a function of all the variables defined in this section: $\eta = \eta\left(\theta_0, \phi_0, \gamma, \Omega, \lambda\right)$. Figure: 11 shows the effect of all those variables on the collection efficiency.

As we can see, due to the crystal symmetry, and the high NA, η has little effect in terms of relative intensities. In other words, only the overall loss of intensity for $\Omega < \pi$ need to be taken in consideration.

The next section will address the technique used in this M. Sc. thesis in order to measure the nonlinear properties of the BBO crystals. As shown in this section, the high NA objective is a key element for the SHG. Since the microscope is mounted in an

Figure 11 – Normalized polarization response for θ=18, 54, 90 degrees (solid, dashed and dotted lines respectively). (a) neglecting the axial component (b) taking into account the axial component of polarization. (1) $\Omega=\pi$ (2) $\Omega \approx 0.31\pi$

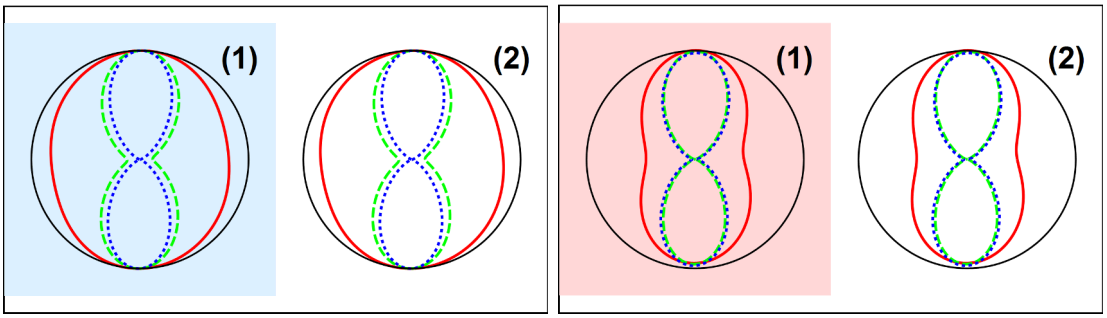

(a) (b)

epi-geometry configuration, the objective will also play an important role at the imaging process and collecting data. Due to the diffraction limits, the image of single emitters will roughly assume the shape of the so called **Point Spread Function** (PSF).

2.2 Theory of Confocal Microscopy

After presenting the origins of SH polarization wave for a single BBO nanocrystal, we direct our attention to the imaging process of the microscope. Starting from some key definition in confocal microscopy, we show how the resolution depends on the imaging process and the pinhole size (CORLE; KINO, 1996a; CORLE; KINO, 1996b). The SH alone gives a better resolution power when compared to reflection or fluorescence, but the main gain of resolution comes from a properly chosen pinhole size. For this M. Sc. thesis, the pinhole size is ideal for wavelength and the objective's specifications, thus the imaging process can be explored in full extent.

2.2.1 Basic definitions for confocal microscopy

Definition 2.4 (Point Spread Function)**.** *The PSF is defined as the image amplitude at the detector plane when the lens is illuminated by a perfectly point light source. Diffraction and aberrations will make the point light source appears like a blur of finite area.*

The PSF is a function of several variables, not only the spatial coordinates but also the microscope's parameters such as the NA, incident wavelength and in case of oil immersion objectives, the oil's refractive index. Therefore, it is useful to introduce normalized optical units so the number of variables can be reduced thus optimizing computer simulations.

Definition 2.5 (Normalized Optical Units)**.** *The Optical Unit (OU) is a dimensionless units of length used in optical microscopy. There are actually two units, one axial (u), along the optical axis of the objective and one radial (ν), along the detector plane.*

$$u = \frac{n\pi z}{\lambda}\left(1 - \cos\theta\right) \tag{2.37}$$

$$\nu = \frac{2\pi r}{\lambda}\frac{n\sin\left(\theta\right)}{M}, \tag{2.38}$$

where n is the refractive index between the objective and the sample; λ is the incident wavelength; θ is the cone angle; M is the total magnification , taken as 1 if we are interested in the sample size. z and r are ordinary lengths. OU can easily be rewritten in terms of wavenumbers: $k \equiv \frac{2\pi}{\lambda}$.

Definition 2.6 (Epi-geometry and transmission geometry)**.** *In epi-geometry, the light scattered by the sample is collected by the same objective, while in transmission geometry, a second objective is placed in order to collect the signal. It is also possible to put a second objective in a right angle or in any intermediate position (ZUGEL; LYTLE, 2000).*

2.2.2 The technique

Confocal microscopy (CM) is often performed under tight focusing conditions given by a high NA objective. To collect the signal, several arrangements are possible. Epi-geometry has some advantages, like the less complicated alignment and the imaging theory is straightforward. In contrast, the transmission geometry can optimize both excitation and collection by means of an ideal objective for each task. Figure 12(a) shows the image formation in both geometries, assuming a process in which the emission occurs in a shorter wavelength.

Figure 12 – Confocal microscopy. (a) Excitation and collection spots for reflection (epi-geometry) and transmission geometries. C is the coverslip, where the sample is placed. (b) Basic experimental setup.

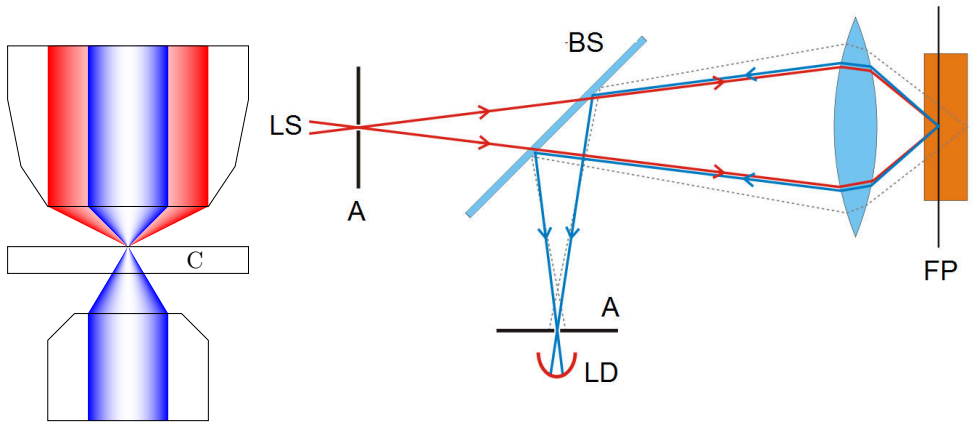

(a) (b)

The basic setup of a Confocal Scanning Optical Microscope (CSOM) under epi-geometry configuration is shown in Figure 12(b). The light scattered by the sample is

collected through the objective and an ideal beamsplitter (BS) ensures that only the wavelengths of interest hit the aperture (A) and the light detector (LD). The confocal character of the microscope is given by the aperture (pinhole), for the signal coming from regions out of focus in the focal plane (FP) will not be able to hit the LD.

Table 2 – Differences between the conventional microscope and the CSOM

System	Illumination	Image amplitude	Intensity	Radial resolution (FWHM)
Conventional	Incoherent	$A_S(r) = h(r)$	$I_S(r) = \lvert h(r)\rvert^2$	$d_{Sr} = \frac{0.51\lambda}{NA}$
CSOM	Coherent	$A_C(r) = h^2(r)$	$I_C(r) = \lvert h^2(r)\rvert^2$	$d_{Cr} = \frac{0.37\lambda}{NA}$

Table 2 shows a brief summary of the characteristics of CM, as a comparison to the conventional microscopy. As will be demonstrated in the next section, the conventional microscope can be taken as the limit case of the confocal microscope when the apperture shown in Figure 12(b) is much larger than the typical confocal parameters. The intensity of both the conventional and CSOM is determined by the Airy function $h(r)$:

$$h(r) = \frac{2J_1(\nu)}{\nu} \tag{2.39}$$

The Airy function corresponds to the diffraction pattern that arises when a point object is imaged through the optical system in the paraxial approximation (SÁNCHEZ, 2016). That is, a uniformly-illuminated circular aperture that passes a converging uniform spherical wave yields an Airy function image at the focal plane. For the CSOM, the pinhole generates an effective PSF given by the square of the PSF for a standard microscope, thus resulting in a narrower intensity profile.

Figure 13 – Total PSF for the SH.

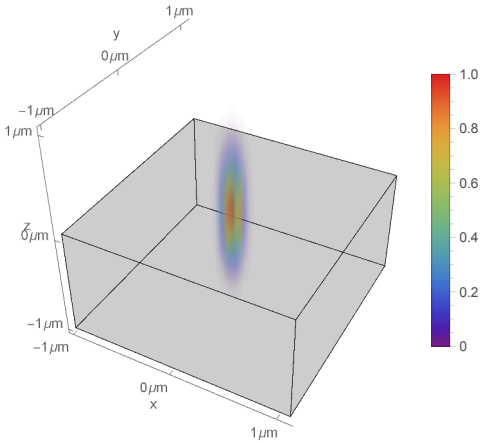

Figure 14 – Total PSF for the fundamental wave.

Figure 15 – Total PSF compared to the coverslip thickness. In this picture, the gray region is 17μm thick or about $\frac{1}{3}$ of the thickness of a sheet of paper.

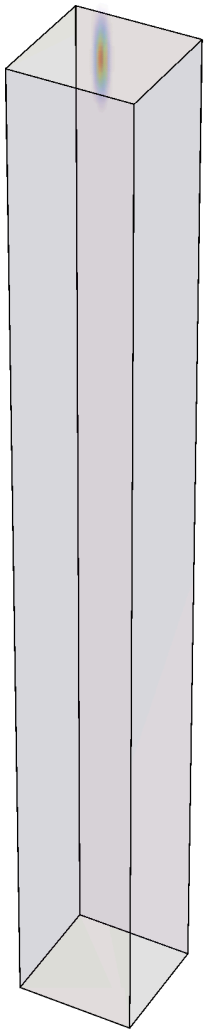

Figure 13 shows the total PSF for the SH, considering both the axial and radial components. It is evident that the under tight focusing conditions, as given by a high NA objective, the signal is only detected within a small focusing volume, when compared to the fundamental wave in Figure 14. The focal volume in which the intensity is half the maximum for the SH is $\approx 3 \cdot 10^{-3} \mu m^3$, for NA=1.25 and λ=820 nm. Figure 15 shows a comparison between the focal volume of the PSF and $\frac{1}{10}$ of the coverslip thickness (170 μm).

2.2.3 Theoretical calculation of the resolution

The rigorous treatment of the CSOM requires that we take into account two main factors: i) the nature of the imaging process (*i. e.*, whether the image is formed by reflection or fluorescence) and ii) the size of the pinhole (*i. e.*, whether the dimensions are relevant in terms of the normalized OU). The ideal pinhole should maximize the collected signal without harming too much the resolution power of the microscope (SANDISON et al., 1995; WILSON; CARLINI, 1987). If the sample can be treated as individual point reflectors at a distance z to the focal plane of the lens, the amplitude of the depth response is given by (CORLE; KINO, 1996c):

$$I\left(z\right)^{p} = \left[\frac{\sin\frac{knz}{2}\left(1-\cos\theta\right)}{\frac{knz}{2}\left(1-\cos\theta\right)}\right]^{4}, \tag{2.40}$$

where k is the wavenumber, n the refractive index, z, the axial position with respect to the focus, and θ the cone angle. Meanwhile, the resolution for a single reflector point is given by:

$$d_{z}^{p} = \frac{0.62\lambda}{n\left(1-\cos\theta\right)} \tag{2.41}$$

A distinct characteristic of CSOM is the small value of d_z^p, so the portions of the sample out of focus are not observed. The intensity of the signal due to individual reflectors is proportional to z^{-4}. Therefore, a large number of particles out of focus has a small contribution to the final image.

For the transverse response for individual reflectors, the amplitude of the PSF is given by $h^2\left(r\right)$ in the paraxial approximation (CORLE; KINO, 1996c):

$$h\left(r\right) = \frac{2J_1\left(kr\sin\theta\right)}{kr\sin\theta}, \tag{2.42}$$

Therefore, we get the usual resolution by the FWHM:

$$d_C = \frac{0.37\lambda}{n\sin\theta_0} = \frac{0.37\lambda}{NA} \tag{2.43}$$

If the sample is composed by fluorescent particles, the depth and transverse responses will change, since the excitation and emission wavelengths are different. The amplitude of the PSF in the excitation wavelength λ_1 is denoted by $h_1\left(x,y,z\right)$ and the PSF of the fluorescence wavelength λ_2 is $h_2\left(\frac{x}{\beta},\frac{y}{\beta},\frac{z}{\beta}\right)$, where $\beta = \frac{\lambda_2}{\lambda_1}$. Assuming that the fluorescence signal is proportional to the pump intensity, the normalized detected intensity profile as a function of the out of focus position is given by:

$$I\left(z\right)_{F}^{p} = \left\{\frac{\sin\left[\frac{k_1 n_1 z}{2}\left(1-\cos\theta\right)\right]}{\frac{k_1 n_1 z}{2}\left(1-\cos\theta\right)}\right\}^{2} \times \left\{\frac{\sin\left[\frac{k_2 n_2 z}{2}\left(1-\cos\theta\right)\right]}{\frac{k_2 n_2 z}{2}\left(1-\cos\theta\right)}\right\}^{2}, \tag{2.44}$$

meanwhile, the normalized intensity for the radial distance in optical units is given by:

$$I\left(\nu\right)_{F}^{p} = \left\{4\left[\frac{J_1\left(\nu\right)}{\nu}\cdot\frac{J_1\left(\frac{\nu}{\beta}\right)}{\frac{\nu}{\beta}}\right]\right\}^{2}, \tag{2.45}$$

Figure 16 represents a simulation of the PSF according to equations 2.44 and 2.45. We note that the ideal situation is obtained for β=1, which is equivalent to the previous case (reflection) (WILSON, 1989).

Figure 16 – Lateral and axial PSF for λ_1=410 nm, NA=1.25 e n=1.5. (a)–(c) are the radial PSF for $\beta = 2$, $\beta = 1$ and $\beta = \frac{2}{3}$ respectively screened across 1 μm^2; (d)–(f) are the corresponding axial PSF for a focus range of 1 μm in both directions.

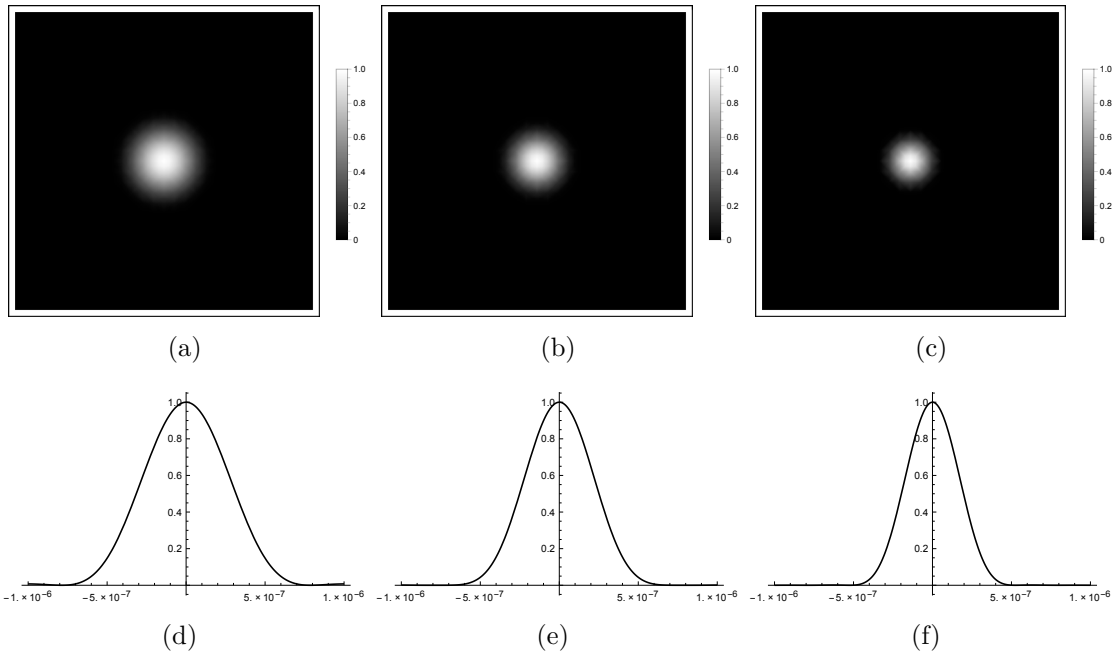

For non linear optics, the Second and Third Harmonic microscopy allows a better intrinsic resolution of the apparatus. In this case, the images are formed coherently due to parametric nature of the optical conversion. For the Second Harmonic Generation (SHG) we have (TANG; XING; LIU, 2004):

$$I_{SHG}\left(\nu_x, \nu_y, 0\right) = \left[\frac{2J_1\left(\sqrt{\nu_x^2 + \nu_y^2}\right)}{\sqrt{\nu_x^2 + \nu_y^2}}\right]^4 \times \left[\frac{2J_1\left(\sqrt{4\nu_x^2 + 4\nu_y^2}\right)}{\sqrt{4\nu_x^2 + 4\nu_y^2}}\right]^2 \tag{2.46}$$

$$I_{SHG}\left(0, 0, u\right) = \left[\frac{\sin\frac{u}{4}}{\frac{u}{4}}\right]^4 \cdot \left[\frac{\sin\frac{u}{2}}{\frac{u}{2}}\right]^2 \tag{2.47}$$

and for the Third Harmonic Generation (THG):

$$I_{THG}\left(\nu_x, \nu_y, 0\right) = \left[\frac{2J_1\left(\sqrt{\nu_x^2 + \nu_y^2}\right)}{\sqrt{\nu_x^2 + \nu_y^2}}\right]^6 \times \left[\frac{2J_1\left(\sqrt{9\nu_x^2 + 9\nu_y^2}\right)}{\sqrt{9\nu_x^2 + 9\nu_y^2}}\right]^2 \tag{2.48}$$

$$I_{THG}\left(0, 0, u\right) = \left[\frac{\sin\frac{u}{4}}{\frac{u}{4}}\right]^6 \cdot \left[\frac{\sin\frac{3u}{2}}{\frac{3u}{2}}\right]^2 \tag{2.49}$$

where ν_x, ν_y e u are given in optical units. Both SHG and THG break the the resolution limit of reflection because the non linear effects make the detection spot smaller than the

excitation one. Figure 17 represents a simulation of the PSF built according to equations 2.40–2.42 and 2.46–2.49. As expected, the resolution increases considerably for the second and third harmonics. It is worth noticing that the harmonics are only visible when the excitation surpasses a certain threshold. In other words, only within a small focal volume the signal will be observed, loosing intensity rapidly outside this region.

Figure 17 – Lateral and axial PSF for λ=820 nm, NA=1.25 e n=1.5. (a)–(c) are the radial PSF for ω, 2ω and 3ω respectively screened across 1 μm^2; (d)–(f) are the corresponding axial PSF for a focus range of 1 μm in both directions.

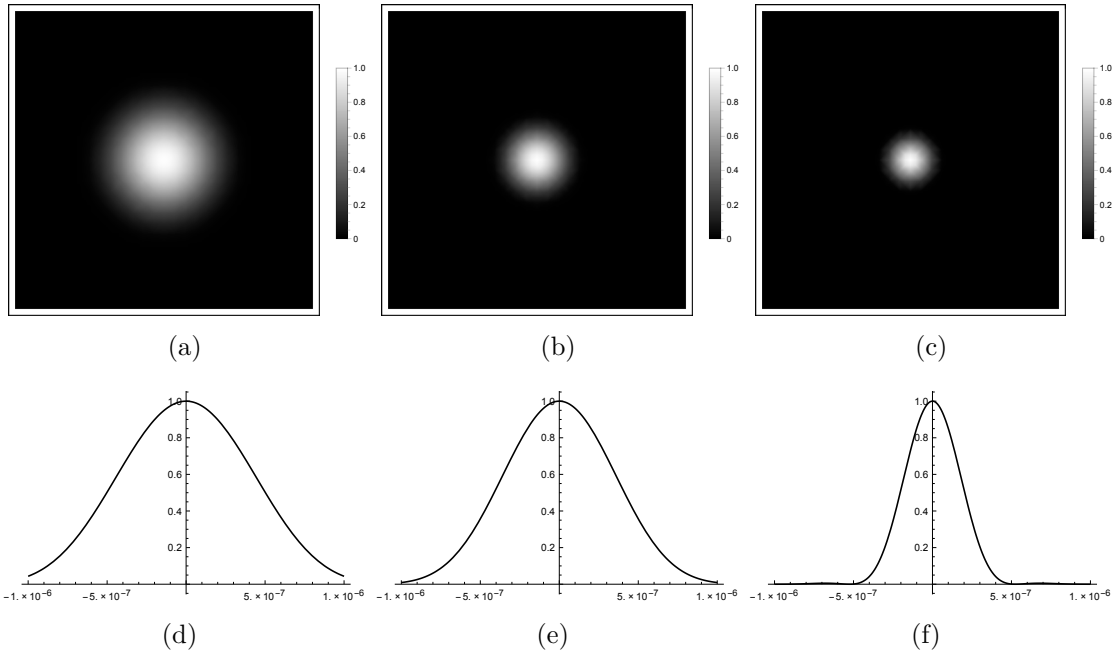

It is important to investigate if there is any symmetry between the processes of harmonics generation and fluorescence. Taking $d_l^H(\lambda, n)$ e $d_l^F(\lambda, \beta)$ the lateral resolutions for the those processes respectively and $d_l^R(\lambda)$ for individual reflectors (equation 2.43), we get:

$$d_l^H(\lambda, n = 1) = d_l^R(\lambda) \tag{2.50}$$

$$d_l^F(\lambda, \beta = 1) = d_l^R(\lambda), \tag{2.51}$$

since the fundamental wave is seen simply as a reflection of light by the particle and β=1 makes a image by fluorescence with identical to the one generated by reflection. Using the same constants employed previously, we get numerical results shown in Figure 18. There, we see that the different imaging processes result in different values for the FWHM of the PSF. Taking as reference the values obtained for the reflection for each wavelength the contraction of the FWHM for the second and third harmonics is not exactly equal to the analogous fluorescence process. For instance, in the second harmonic generation, the ratio between the detected spot and the excitation one is $\approx$0.6 and for the fluorescence the inverted ratio is $\approx$0.8.

In order to introduce the effects of the finite sized pinhole in the resolution, the use of normalized OU simplifies the computational routine. The pinhole's finite size for the lateral resolution is introduced by a piecewise function as follows (WILSON; CARLINI, 1987):

$$I(\nu) = \begin{cases} I(\upsilon) = |h(\nu)|^2 \left[2\pi \int_0^{\nu_p - \nu} |h(t)|^2 \, t dt + 2 \int_{\nu_p - \nu}^{\nu + \nu_p} |h(t)|^2 \times \cos^{-1} \left(\frac{t^2 + \nu^2 - \nu_p}{2t\nu} \right)^2 t dt \right] & \nu < \nu_p \\ I(\upsilon) = 2 |h(\nu)|^2 \int_{\nu - \nu_p}^{\nu + \nu_p} |h(t)|^2 \times \cos^{-1} \left(\frac{t^2 + \nu^2 - \nu_p}{2t\nu} \right)^2 t dt & \nu > \nu_p \end{cases} \tag{2.52}$$

where ν_p is the pinhole radius and t is an integration parameter.

Figure 18 – A comparison among several imaging processes in CSOMs for NA=1.25 and n=1.5. The graph, in order of width from left to right we have: R(273), THG(820–273), F(820–273), R(400), SHG(820–410), F(410–820), R(800), where the letters stand for the imaging process R=Reflection, THG=Third Harmonic Generation, SHG=Second Harmonic Generation and F=Fluorescence. The numbers between parenthesis are the corresponding wavelengths. The dotted line represents a half maximum intensity, so the radial position at half maximum for each curve is half the FWHM.

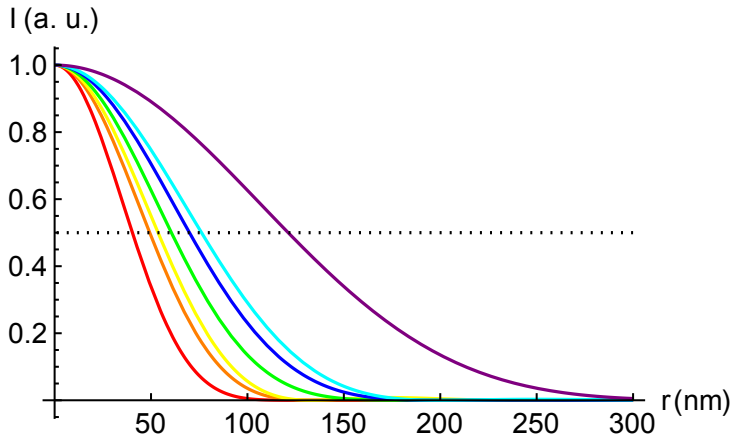

After computing $I(\nu)$, the resolution is determined by solving $I(\nu) = 0.5$ for a given value of ν_p. Figure 19 shows the FWHM calculated for reflection, SH, TH and fluorescence for β=2. For all imaging processes, there is a certain pinhole size for which the resolution is the worst. An improper choice of pinhole size can lead to a decrease in resolution below the conventional microscope's and therefore must be avoided. For this M. Sc. thesis, we used a 0.5 OU pinhole, small enough so the confocal parameters are still preserved.

Considering the limiting case in which the pinhole radius is zero, the confocal resolution is bigger than conventional by a factor of $\sqrt{2}$. Below 0.5 OU, the resolution is not substantially increased and it is almost constant (WILSON; CARLINI, 1988). The results from Figure 19 are also shown in Table 3. It is clear that we reproduce the results of Table 2. In other words, the bigger the size of the pinhole, the closest we get from the conventional microscope (WILSON, 2011). The pinhole size is more critical for nonlinear optical imaging, since above 1 OU for ν_p the resolution quickly shifts to the conventional.

Figure 19 – Lateral resolution of the CSOM as a function of the pinhole size. Dash-dot line is a fluorescence process with $\beta = 2$, solid line is a simple reflection, dashed (dotted) line is the resolution for the second (third) harmonic. $\nu_{1/2}$ is the half FWHM and ν_p is the pinhole size, both given in OU. For ν_p>10 OU, the pinhole is so big that effectively we have a conventional microscope.

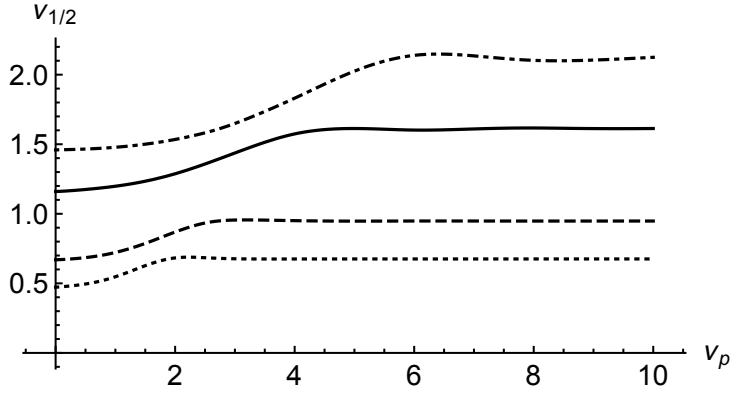

Table 3 – Resolution of the CSOM as a function of the pinhole size

	Fluorescence (β=2)	Fundamental	SH	TH
$\nu_p = 10$	$\frac{2.12}{\pi} \approx \frac{0.68\lambda}{NA}$	$\frac{1.61}{\pi} \approx \frac{0.51\lambda}{NA}$	$\frac{0.95}{\pi} \approx \frac{0.30\lambda}{NA}$	$\frac{0.68}{\pi} \approx \frac{0.21\lambda}{NA}$
$\nu_p = 0$	$\frac{1.46}{\pi} \approx \frac{0.46\lambda}{NA}$	$\frac{1.16}{\pi} \approx \frac{0.37\lambda}{NA}$	$\frac{0.67}{\pi} \approx \frac{0.21\lambda}{NA}$	$\frac{0.47}{\pi} \approx \frac{0.15\lambda}{NA}$

Given the numerical results for the PSF for individual particles, SH and TH microscopy have an intrinsic advantage in terms of resolution, so it is possible to study individual particles at the nanoscale, avoiding the ensemble averages. In that limit, phase-matching is not relevant, so the signal can be easily tunable to a wide range of frequencies. Decreasing the excitation wavelength (*ceteris paribus*[2]) the resolution of the microscope increases, but the collected signal will start to be shifted to the ultraviolet range, more difficult to detect.

For fluorescent particles, the excitation wavelength is often limited by the kind of organic molecule used as fluorophore, so a gain in resolution is easier to obtain by choosing a smaller pinhole or a larger numerical aperture. We can see in Table 3 that the size of the pinhole alone is responsible for an increase in resolution by a factor of $\frac{2.12}{1.46} \approx \sqrt{2}$. The value of the FWHM for β= 2 resides in a intermediate position between the larger fluorescence spot at 2λ and the smaller excitation spot at λ, since both components participate in the generation of the detected profile intensity.

[2] *Id est*, keeping the other variables such as the pinhole size constant.

3 EXPERIMENTAL RESULTS

3.1 Experimental setup

In the previous chapter, we showed how the second harmonic is generated for a single β–BBO nanocrystal as well as some considerations about the imaging process in CSOMs. In this section we present the experimental setup in more detail.

3.1.1 Setup description

The experimental setup shown in Figure 20 is as follows: A mode-locked Ti:Sapphire laser (120fs, 76MHz, Mira Model 900-F Coherent) is set at 820 nm and it is directed to a telescope in order to compensate laser beam divergence. The cavity is optimized for a maximum output intensity. In the telescope's focal position, a chopper is installed in order to modulate the laser at a fixed frequency, given by the chopper's controller. The frequency is adjusted to be about 2 kHz and kept away from any possible harmonic of the electrical power supply frequency (*i.e.*, 60 Hz).

Following the path, the laser goes through a half-wave plate and a polarizer, that allows the intensity control for a given polarization, which will be important for some measurements. The laser beam then passes through a second half-wave plate mounted on a rotatory mount. At this point, the choice of the wavelength of the laser at 820 nm is evident: the dichroic mirror DMSP805 (Thorlabs) available for this experiment has an optimal reflection for wavelengths larger than 810 nm and a good transmission around 410 nm, so a SH generation for 820 nm would be ideal for both processes and yet keeping the laser cavity stable.

All the mirrors in the experiment up to this point are dielectric BB1-E03 (Thorlabs), so a reflection >99% is achieved. Beyond the beamsplitter, all the other mirrors are metallic (aluminum) for a better signal reflection. After entering in the inverted microscope, the laser is focused by a 100× DIN Achromatic Commercial Grade Objective, oil immersion, NA=1.25 (Edmund Optics). A 18×18 mm cover glass is set on top of the objective held in place by magnets over a metallic support. The sample is moved in three directions by the piezo module NanoMax 300 (Thorlabs), while the laser source is kept in a fixed position.

After the particle is placed in the focal spot, the SH signal (plus the fundamental frequency) travels back through the same objective and is transmitted by the dichroic mirror, shining on another telescope at which focal point is a 10 μm pinhole P10S (Thorlabs) installed. After that, the signal can go to a photomultiplier route or an APD route. In the PMT route, a DoubleMate monochromator is used for measurements of the spectra of the light emitted by the nanocrystals, which is detected by a H9305 (Hamamatsu) PMT. At the APD route, a MiniMate monochromator is used as a filter to eliminate

Figure 20 – Setup employed in the experiments. M1–M3 are dielectric mirrors, M4–M12 are metallic mirrors, W1 and W2 are half-wave plates, L1–L4 are convex lens, D is a dichroic mirror acting as a beamsplitter, PH is a pinhole, PD is a reference photodiode and BS is a simple beamsplitter composed of a thin glass slab.

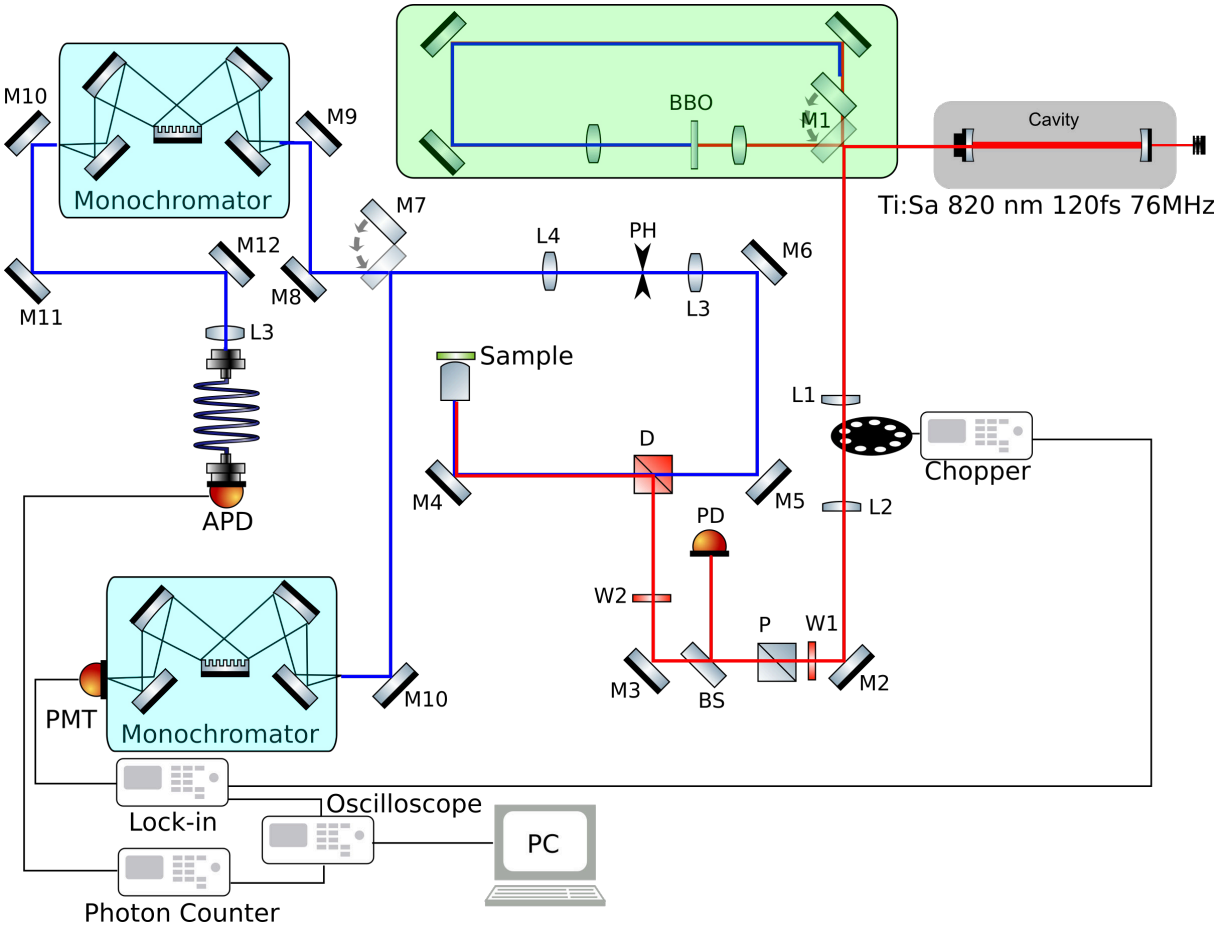

undesired scattered light going to the APD. The light if focused by an achromatic lens and it is coupled to the APD module by a multimode optical fiber, which achieves a more efficient light coupling due to the larger core diameter. The APD route was thought as a way to detect weaker signals, since it combines a single photon detector SPCM-AQR-12 (PerkinElmer) and a monochromator with only one diffraction grating.

In the PMT route, the PMT is connected to the SR510 Lock-in Amplifier (Stanford Research Systems). Essentially, a lock-in is a filter with a narrow bandwidth which is tuned to a frequency at which the signal is being modulated. Such a filter will reject most unwanted noise to allow the signal to be measured. Both the PMT and the lock-in introduce an enormous gain factor to the SH signal, allowing it to be easily discernible from the noise. The lock-in is set by the chopper modulation and the output is connected to a 2424C Oscilloscope (Tektronix). Similarly, at the APD route, the APD is connected to a SR400 Gated Photon Counter (Stanford Research Systems) and then to the oscilloscope.

In order to do a raster scan, the oscilloscope is set as a measuring device, in which

the first input is reserved for DC signals coming from the lock-in amplifier or the photon counter. The second input in the oscilloscope shows the reference slow photodetector, properly calibrated to the laser intensity at the sample. The photodetector is protected from saturation by a color filter. The piezo is controlled by a MDT693B Open-Loop Piezo Controller (Thorlabs) and the whole communication is set by software. The simplest measurement that can be made in this setup is the emission spectrum for the SH. For this kind of measurement, a stepper motor is put in the DoubleMate in the PMT route and the communication between the stepper motor driver and the oscilloscope is also set by software.

During the measurements, it is possible to optimize the particle's position manually in the piezo as well at the piezo controller; the spectrum can be recorded once the particle is located; the signal intensity can be correlated to the angle of the second half-wave plate and a 2D or even 3D images can be obtained at a desired wavelength for a single particle. On the other hand, the full operation of the setup is no easy task. Firstly, the correct alignment of all components is critical, since the inverted microscope relies on the perpendicularity of the laser and the correct positioning of all components. Secondly, due to the nature of the parametric process, nonlinear signals are only seen for a tiny focal volume, and even so, the signal is very weak. A correct balance between the gain factors need to be set as well as a proper integration time in the equipments. A drawback of the communication between the computer and the instruments is speed, which only allows one pixel be recorded for every 100 ms.

There are also other intrinsic limitations of the apparatus. The piezo goes only as far as 20 μm for the full range of 75V that can be applied. So, effectively, the raster scan is limited by 10 μm for the left and right assuming that the particle is perfectly positioned at the middle, which is not always possible to achieve. Due to the communication limitation, small areas (about 9-25 μm^2) were chosen for raster scanning, since one full measurement of a single particle can take a couple hours. A faster raster scan results in poor quality image, since acquisition is limited by the communication speed and the integration time.

3.1.2 Calibrating the setup

In order to check the accuracy of the system, some tests were made before investigating SHG in single BBO nanocrystals. By making a detour at the laser right on the first mirror (green region in Figure 20), it is possible to generate light at 410 nm with a 0.1 mm thick BBO crystal. The light is then directed again to the original path and the spectrometers can be calibrated. The reads on the DoubleMate and MiniMate are checked against a standard Ocean Optics table spectrometer (HR4000CG-UV-NIR) for three different wavelengths: 410, 532 and 820 nm[1]. In general, the DoubleMate had a very good agreement

[1] 820 nm is the fundamental frequency, 410 nm is the SH generated by the 0.1 mm BBO crystal and 532 nm is an ordinary CW green laser.

Table 4 – Values of w_0 and FWHM in nm for the three wavelengths in Figure 21.

Figure 21	410		532		820	
	w_0	FWHM	w_0	FWHM	w_0	FWHM
(a) DoubleMate monochromator	1.28	3.00	1.16	2.73	2.84	6.67
(b) Ocean Optics Spectrometer	0.41	0.96	0.37	0.87	3.26	7.66

with the reference spectrometer, being off by about a couple of nanometers, as shown in Figure 21. On the other hand, the MiniMate had a much larger offset, about 20 nm of discrepancy, showing readings above the true value of the wavelength. For each spectrometer, a calibration curve was built. For reasons shown in Section 3.4, only the DoubleMate data will be taken in consideration.

Figure 21 – Setup calibration. (a) DoubleMate monochromator; (b) Ocean Optics Spectrometer. In both pictures from left to right is shown the SH generated by the 0.1 mm thick BBO crystal, the green CW laser and the fundamental Ti:Sa laser. In (a) this reads are 410.40, 535.32 and 821.92 nm respectively and in (b) the reads are 409.16, 531.35, 818.59 nm respectively. Values taken for the maximum intensity in arbitrary units (a. u.).

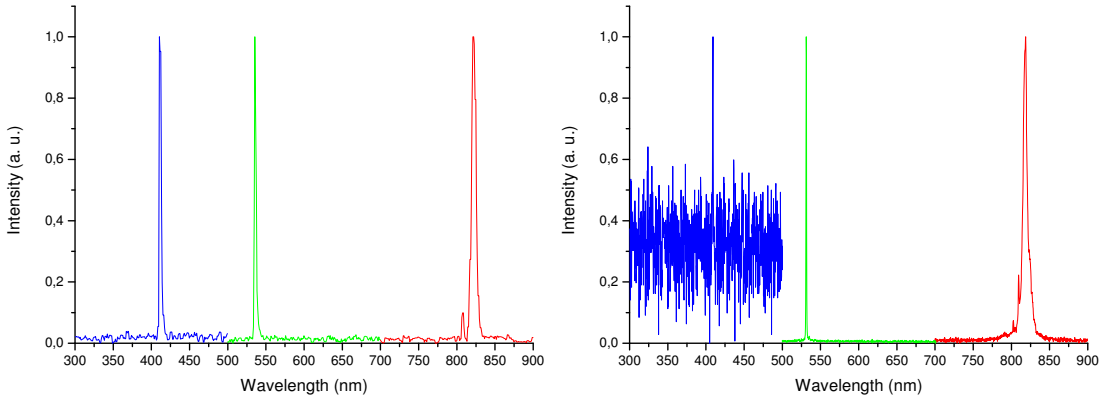

(a) (b)

We notice from Figure 21 that a PMT is crucial for detecting the weak SH signals coming from single emitters, since the Ocean Optics spectrometer has a poor S/N ratio for the SH. We also notice a shortening in the laser's width for the SH, as expected. From a Gaussian fit, it can be shown that the FWHM is related to the variance as follows:

$$FWHM = 2w_0\sqrt{2\ln 2} \approx 2.35w_0, \tag{3.1}$$

where w_0 is the standard deviation considering a Gaussian distribution. Table 4 shows the values of w_0 and the $FWHM$ for the three wavelengths measured in Figure 21. The 532 nm laser can be taken as a reference width, for it is a narrow CW light source. Therefore, the DoubleMate monochromator has a resolution of 2–3 nm (FWHM), while the Ocean Optics Spectrometer has a resolution of <1 nm (FWHM), exactly as the technical specifications.

3.2 The sample

The samples were synthesized and characterized by Professor Lauro Maia's research group at Universidade Federal de Goiás. Among the characterization techniques used, X-ray diffraction at Bragg–Brentano θ-2θ configuration. Results are shown in Figure 22. The same picture shows the data from JCPDS 80-1489 for the β–BaB_2O_4 diffraction patterns. We notice that a single crystalline phase is seen. The β–BBO phase is a rhombohedral structure being non-centrosymmetric and present non linear properties, as described in page 19 of this M. Sc. thesis.

Figure 22 – The X-ray diffraction (XRD) measurements taken with a Shimadzu XRD-6000 X-ray diffractometer with Bragg-Brentano θ-2θ geometry, at a continuous scan speed of 1°/min from 10° to 60° with sampling pitch of 0.01°. K_α radiation of 1.54059 Å from a Cu tube operating at 40 kV was used.

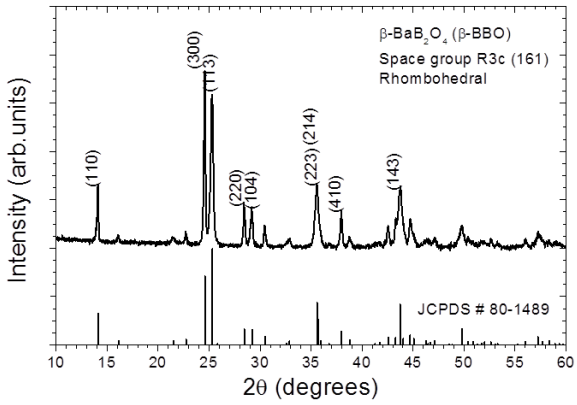

Figure 23 shows the Transmission Electronic Microscopy (TEM), High-Resolution Transmission Electronic Microscopy (HR-TEM) and the Selected Area Electron Diffraction (SAED) images of a typical sample from the same batch as used during the SHG experiments. As can be seen, the BBO particles are shaped as needles. This is a result of the crystals' growth process, in which the crystals grow along the c-axis, thus making one dimension much bigger than the other two. On the other hand, the SAED image shows that the needles are polycrystalline, because they show a continuous ring around the observed area, without showing any bright spot, typical of monocrystalline samples. This can also be verified in the HR–TEM images, where interference fringes of crystallites about 10 mm in diameter can be seen inside a single needle.

Those crystallites are also a consequence of the growth process, but since they do not alter the c-axis orientation, the defects are invisible to the SHG imaging technique: The needles are effectively seen as a monocrystalline regardless of the defects. Figure 24 shows the needles' length dispersion. From the histogram, we notice that the most probable sizes are about 100-150 nm, although crystals as big as 1 micron can be found. This result was also found in SEM images made with MIRA3 TESCAN Scanning Electron Microscope, showing individual particles as big as 1 micron. The bigger crystals are useful for the

Figure 23 – (a) and (b) Transmission Electronic Microscopy (TEM) images of some structures, (c) High-Resolution Transmission Electronic Microscopy (HR–TEM) image of an individual structure showing two crystallites; (d) Selected Area Electron Diffraction (SAED) image of β-BBO powder.

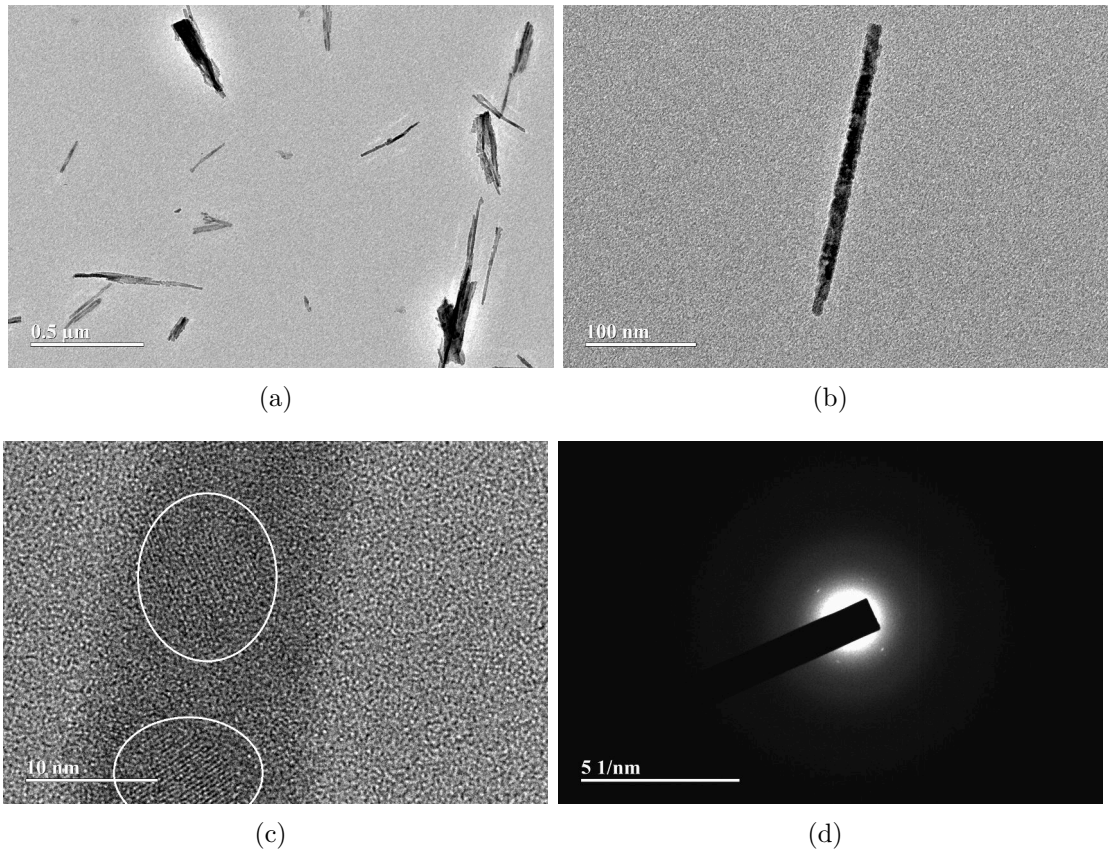

(a) (b)

(c) (d)

experiment because at that size the PSF is small enough to start forming a sharper image, as will be shown in the next section.

Figure 24 – Needles' size dispersion. The most probable lengths are about 100-150 nm, although crystals as big as 1 micron can be found.

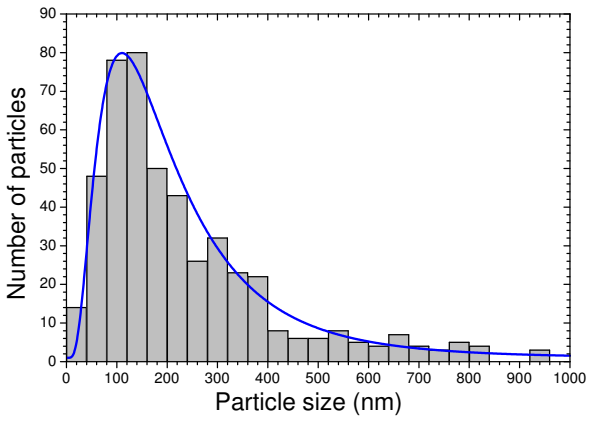

The diffuse reflectance spectra were obtained using a UV–Vis–NIR PerkinElmer Lambda 1200WB spectrophotometer and a Praying Mantis accessory. $BaSO_4$ powder from

Sigma-Aldrich was used as standard reflectance material. We notice a huge *plateau* located from 400 to 1200 nm, which is the limit of the data. This *plateau* suggests that the sample is transparent all the way through that region of the electromagnetic spectrum. The drop of reflectance in the ultraviolet suggest a significant absorption of the light below 400 nm (MIRANDA, 2016).

Figure 25 – Diffuse reflectance. $BaSO_4$ powder from Sigma-Aldrich was used as standard reflectance material.

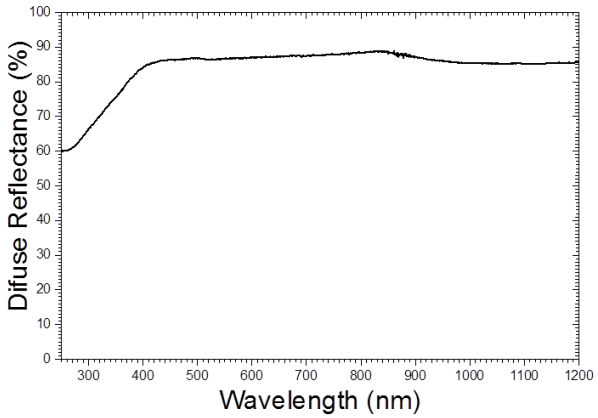

3.3 Making sure that the nanocrystals are individual

As shown before, the signal's polarization response is able to discern the orientation of nanocrystals and therefore whether one observes single crystals or clusters. The distinct polarization signature of a single crystallographic c-axis ensures an individual emitter. That kind of measurement is beyond the limits of direct observation, since the excitation laser is diffraction limited. On the other hand, a much shorter wavelength can be achieved using an electron microscope, so a direct measure of the shape of the crystals is possible. The sample is prepared depositing an isopropanol suspension (1 mg/ml) in 10 μl aliquots of a batch previously put in an ultrasonic bath for 20 minutes. The MIRA3 TESCAN SEM showed individual crystals for this deposition parameters and in order to keep the crystals fairly close together, one drop of the suspension is let dry, so the concentration is still high enough for an easy scanning and yet the clusters are split by the ultrasonic bath.

Using the images collected by the MIRA3 TESCAN SEM, it is possible to predict the behavior of the PSF once the confocal parameters are changed. Converting the crystal's image to an 8-bit grayscale, each pixel can be approximated as an infinitesimal emitter, so a PSF distribution can be attributed for each pixel. Figure 26 shows the simulation results. It is shown that under the confocal configuration, the contours of this 1 micron long particle begin to be resolved. The tradeoff of this gain in resolution is of course a weaker signal. Since the confocal parameters are in normalized optical units, this simulation also

suggests that a nonlinear imaging by itself provides a better resolution when compared to reflection.

Figure 26 – (a) Single nanocrystal as seen by SEM (1 μm yellow bar for scale); (b) The image from (a) is converted into a matrix form. For better visualization, the colors are inverted and only 4 μm^2 are shown. Each small square corresponds to 100 nm; (c) Detected image for a FWHM=100 nm PSF; (c) Detected image for a FWHM=300 nm PSF.

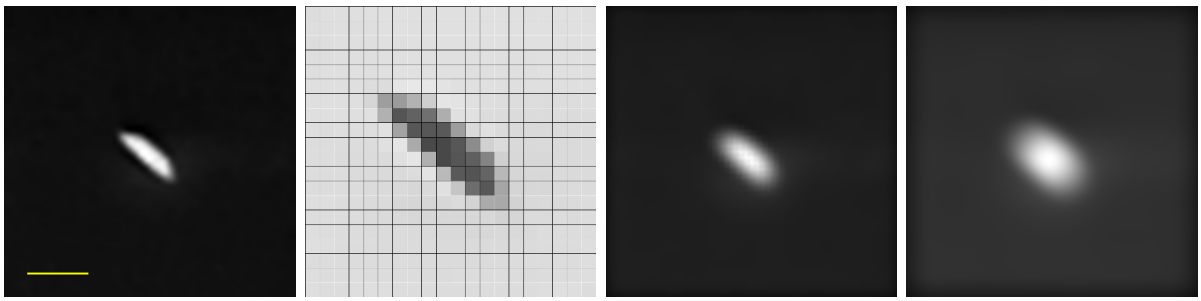

(a) (b) (c) (d)

3.4 Optimizing the signal-to-noise (S/N) ratio

The alignment and fine tuning of the setup is time consuming, since the signal is very weak and in order to properly perform the necessary measurements, a stable and reliable signal is required. Several attempts were made to increase the S/N ratio, first by means of a lock-in amplifier and a chopper, which is able to filter the noise created by spurious light and any other signal out of the expected modulated frequency.

Several attempts were made to optimize the detection setup, like replacing the spectrometer, the photomultiplier, or even changing the PMT for an APD. The change of spectrometer from a DoubleMate to a MiniMate was not effective detecting higher harmonics and only allowed the detection of a larger SH signal. Searching through the available photomultipliers, we noticed that PMT H9305 was already the best suited for the experiment, because of the spectral sensitivity. After considering the results, the best configuration appeared to be the DoubleMate spectrometer and the PMT H9305, set for a high gain while the sensitivity scale at the lock-in is set adequately. Eventual overload intensities are prevented using a set of neutral density filters right at the entry of the monochromator. The laser intensity at the sample is limited only by the losses of the optical components. The integration time is also an important parameter, and can be set during each step of measuring data or at the signal processing in the lock-in itself.

After the apparatus fine tuning, the S/N ratio for the Second Harmonic was enough for the sample's optical characterization, shown in the following sections. On the other hand, the Third Harmonic signal is barely seen even after several attempts of optimization. That result can be attributed to the following limitations:

1. The signal is much more dependent on the pump intensity (third power) and every loss introduced in the path is critical;

2. The signal is generated at a much shorter wavelength (about 273 nm), so specific optical components would be needed to mitigate the signal losses after it leaves the sample;

3. The signal itself is known to be about one order of magnitude weaker than the SH for a number of particles>>1 (MIRANDA, 2016);

4. The PMT is less sensitive at that wavelength when compared to the SH and the fundamental;

5. The APD we tried to use ended up being completely blind for the TH;

6. As shown in Figure 25, around 300 nm the sample starts to absorb a significant amount of light, so the TH of 820 nm will suffer losses in intensity. That also limits the the ultraviolet power output for SHG for shorter excitation wavelengths (DEYRA et al., 2015).

Therefore, the discussion will be limited to the SH, in which the measurements were much more reliable. Furthermore, the SH allows using a pinhole for better resolution, especially when the spectrometer is also set for a high spectral resolution.

3.5 Collecting data

In this section it is shown the experimental routine as performed in a typical measurement. First, the monochromator is set for the expected SH wavelength (410 nm) and the particle is located by a manual scan in the X and Y directions. This first scan also gives a basic idea of the particle's size. Then, the polarization response is recorded to ensure the presence of single emitters. For some particles, the spectrum and raster scan are recorded. Since those two measurements are the most time consuming, they are repeated for a smaller set of particles. The experimental routine is carried out that way due to technical constrains of the setup. The raster scan is not only time consuming but also limited to a small area. Therefore, if the raster scan is performed without the particle being carefully positioned, it is likely that the scan will show no particles whatsoever. Because of circuitry limitations, the spectrum can only be recorded once the piezo communication is terminated.

3.5.1 Polarization response

Using the second half-wave plate in the experimental setup, the polarization response is recorded in a similar way as the spectrum and the raster scan. The plate is rotated up to

a half revolution, at 10 degrees increments, so the wave plate will rotate the polarization direction through an angle 2α, resulting in a full revolution at 20 degrees increments.

Figure 27 – Polarization response for some crystals–I. From (a) to (f) the NCs orientations are: (79°,73°), (79°,94°), (63°,73°), (77°,94°), (67°,82°) and (77°,97°) for (θ_0,ϕ_0).

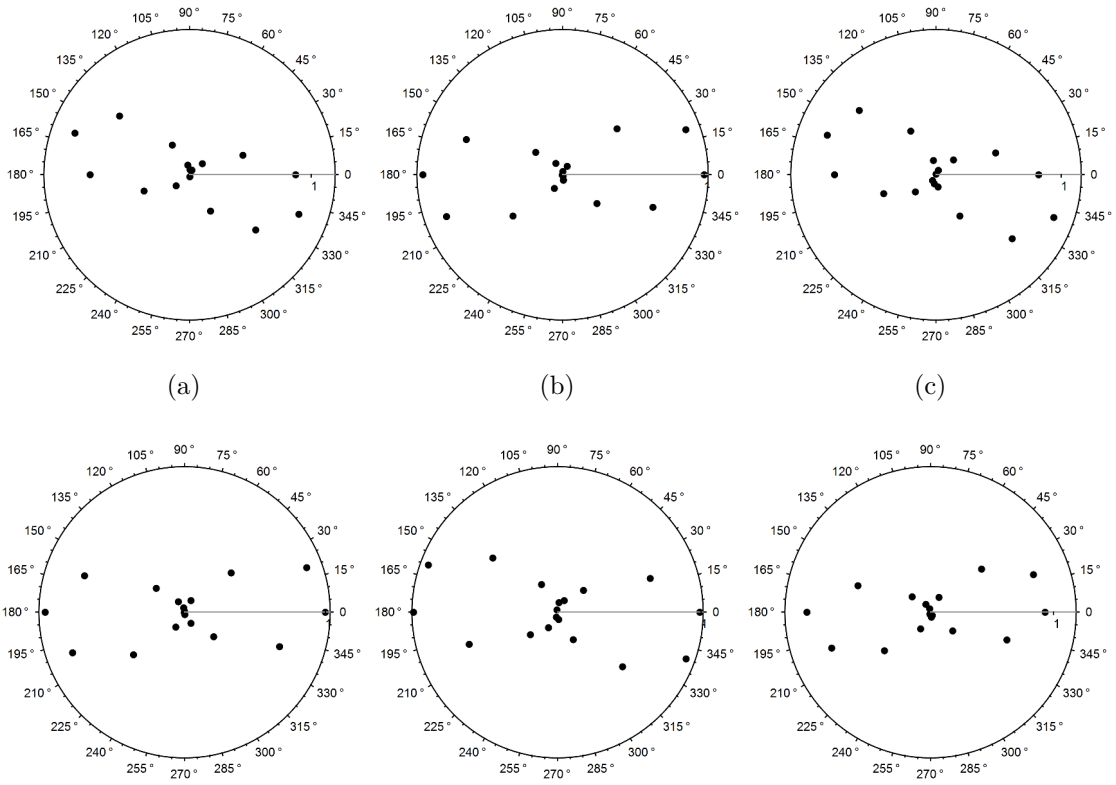

(a) (b) (c)

(d) (e) (f)

During the measurements, it was necessary to take into consideration the dichroic mirror's polarization response. A power meter was positioned just after the dichroic mirror and the pump power was recorded while the waveplate was rotated. Therefore, it is possible to compensate the power losses due to the dichroic mirror polarization response for the SHG experiments.

The polarization measurement is repeated for several crystals and the points were manually fitted for the variables θ_0 and ϕ_0, as shown in Figures 27–28[2]. The figures are already corrected by the power losses introduced by the dichroic mirror. A simple Mathematica code imports the raw data, corrects the intensity for the pump losses and gives the crystal orientation. The single crystals show a distinct polarization signature for every pair of angles, measured relatively to the incident polarization plan.The crystals are said to be individual due to the narrow width of the ∞-shaped curve. A circular polarization pattern would suggest that multiple crystals are seen together in random orientations.

[2] See Figure 7 in page 20 for the NCs orientation.

Figure 28 – Polarization response for some crystals–II. From (a) to (f) the NCs orientations are: (74°,114°), (69°,77°), (80°,111°), (64°,73°), (47°,134°) and (85°,61°) for (θ_0,ϕ_0).

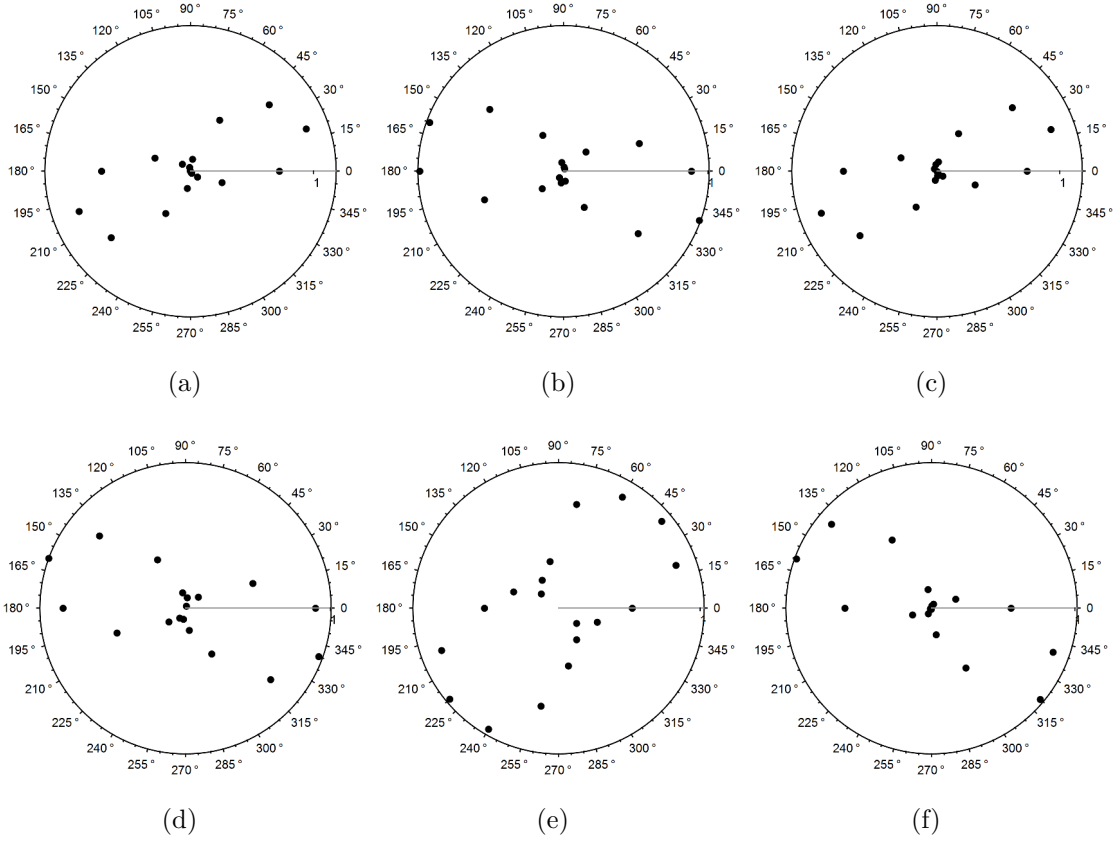

(a) (b) (c)

(d) (e) (f)

We notice that the majority of the crystals are oriented around ϕ_0=90°–270°. It is worth noticing that the crystal orientation is **not** the same as the ∞-shaped curve's. From equations 2.32–2.33, it can be shown that the crystal orientation makes a right angle with respect to the ∞-shaped curve's orientation. The reason for that values for ϕ_0 is quite simple. Since the power irradiated by the NCs is strongly dependent on the incident polarization angle, when the NCs passes through the laser focal spot, only the ones oriented is such a way that the polarization curve gives a sufficient large signal can be detected. This happens because the polarization response is recorded after the particle is positioned and therefore certain orientations are effectively invisible for the initial polarization angle. If it was possible to do a large raster scan for a fixed polarization orientation, we should be able to see a large amount of single NCs, but once the second waveplate is rotated, some of the NCs would look dimmer and some would look brighter. That effect can be compensated by using doped NCs, since the luminescence is not polarization dependent (MAYER et al., 2014).

3.5.2 Spectral data

The total SH radiation power in the electrostatic approximation is given by (HSIEH et al., 2009):

$$W_0^{(2\omega)} = \frac{ck^4V^2}{12\pi\epsilon_0}\left|\mathbf{P}^{(\mathbf{2}\omega)}\right|^2, \tag{3.2}$$

where c is the speed of light, k is the wave number at the SH frequency, V is the nanocrystal's volume and ϵ_0 is the vacuum permittivity. Since:

$$\left|\mathbf{P}^{(\mathbf{2}\omega)}\right|^2 \propto \left[I^{(\omega)}\right]^2 \tag{3.3}$$

Thus:

$$I^{(2\omega)} \propto \left[I^{(\omega)}\right]^2, \tag{3.4}$$

where $I^{(2\omega)}$ and $I^{(\omega)}$ are the signal and pump power respectively. Therefore, a log-log plot correlating those two must show an apparent straight line, since:

$$I^{(2\omega)} = \alpha\left[I^{(\omega)}\right]^2 \Rightarrow \log\left(I^{(2\omega)}\right) = 2\log\left(I^{(\omega)}\right) + \log(\alpha), \tag{3.5}$$

where α is a constant.

As shown in Figure 29, the SH signal is $\propto I^{1.96}$, thus a quadratic power dependence on the pump laser. The S/N ratio is about 1000:1, and so a quite good fit is possible for the power dependence and the system can handle the pinhole without completely loosing the signal. The peak position is 409.5 nm, FWHM=2.68 nm. As seen during the setup calibration, the monochromator has a resolution of about 3 nm so the observed spectrum will be limited solely by the spectrometer resolution. The spectral distribution for nonlinear signals can be expressed as (EHMKE et al., 2015):

$$\Delta\lambda_n = \frac{1}{n\sqrt{n}}\Delta\lambda_{fund}, \tag{3.6}$$

where n is the harmonic order, $\Delta\lambda_{fund}$ is the fundamental FWHM and $\Delta\lambda_n$ is the FWHM for the nth-order harmonic. For SHG we have a narrowing factor of $\frac{1}{2\sqrt{2}}$ ≈0.354. For FWHM of 6.7 nm at 820 nm central wavelength, the FWHM of the second harmonic pulses generated at 410 nm central wavelength should therefore be ≈2.4 nm, which is compatible with the experimental results (2.7 nm).

It is noticeable an asymmetry on the right side of the SH spectrum. That can be a result of some artifacts during the data collection such as vibrations in the diffraction grating introduced by the stepper motor.

In order to get an estimation for the effective nonlinear susceptibility, it is necessary to take into account all the losses introduced by the optical components. We start by calculating the SH power irradiated that can be collected by the objective. For the objective used in this thesis, we get a cone angle $\theta = 0.31\pi$, which gives a solid angle in steradian:

$$\Omega = 2\pi(1 - \cos\theta) \approx 0.87\pi\ sr \tag{3.7}$$

Figure 29 – Spectral data. (a) SH signal. (b) Power dependence. Signals in arbitrary units (a. u.).

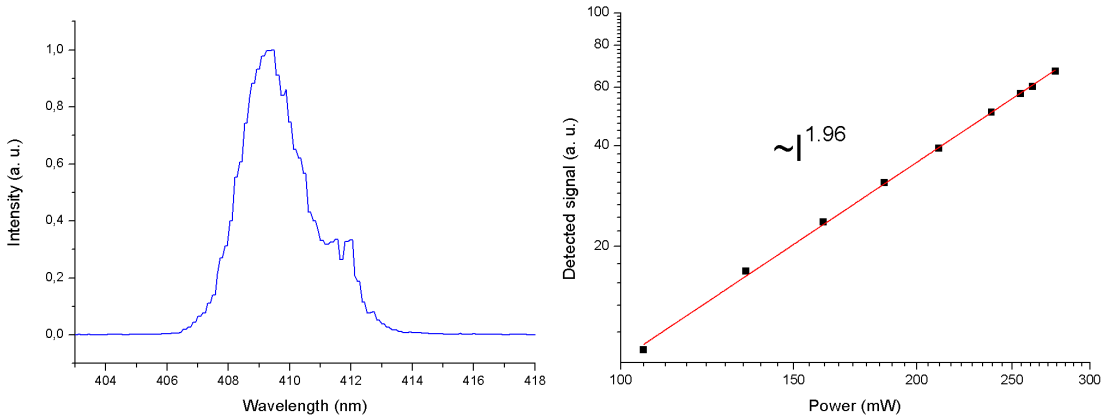

(a) (b)

The solid angle is related to the area it cuts out of a sphere as:

$$\Omega = \frac{A}{r^2}\ sr, \tag{3.8}$$

where A is the surface area of the spherical cap, r is the radius of the sphere, and sr is the unit, steradian. The radius of the sphere is the objective's working distance, 0.1 mm. Thus:

$$A \approx 0.22S, \tag{3.9}$$

where S is the total spherical surface. The geometry is summarized in Figure 30. The working distance is defined as the distance from the front lens of the objective to the closest surface of the coverslip when the sample is in sharp focus.

Figure 30 – Steradian cone in sphere. A is the spherical cap surface area and r the sphere radius, given by the objective's working distance. Assuming an uniform SH power radiation, only 22% of the signal is collected by the objective.

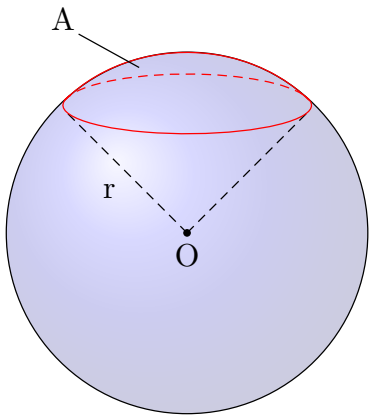

All the losses and gains in signal need to be compensated so the total SH power irradiated by the single nanocrystal can be obtained. The total SH power can be related to an effective nonlinear coefficient, which for BBO can be written as (MIRANDA, 2016):

$$d_{eff} \approx \sqrt{\frac{8d_{22}^2}{21}}, \tag{3.10}$$

where d_{22}=2 pm/V. From Equations 3.2–3.3, it can be shown that (PU; PSALTIS, 2016; HSIEH et al., 2010b):

$$W_0^{(2\omega)} = \sigma_{2p}\left[I^{(\omega)}\right]^2 \tag{3.11}$$

$$\sigma_{2p} = \frac{16\pi}{27}\frac{1}{\epsilon_1}\left(\frac{3\epsilon_1}{\epsilon_2+2\epsilon_1}\right)^4 c^2 Z_0^3 k_2^4 r^6 \left|\mathbf{d}\cdot\hat{\mathbf{e}}\hat{\mathbf{e}}\right|^2, \tag{3.12}$$

where σ_{2p} is the two-photon cross-section (in Göppert-Mayer units), ϵ_1 and ϵ_2 are the dielectric constants of the sphere and surrounding medium respectively, c is the speed of light, Z_0 the vacuum impedance, $k_2 = \frac{2\omega}{c}$, $\hat{\mathbf{e}}$ is the unit vector in the crystal reference frame and r is an effective radius considering a spherical particle. After choosing a convenient nanocrystal orientation, finding d_{eff} is a matter of measuring σ_{2p} and substituting that value in Equation 3.12.

Unfortunately, an accurate estimation for σ_{2p} could not be obtained with the experimental setup. The lock-in amplifier introduces a gain factor difficult to be controlled without a reference signal. Moreover, the losses in SHG need to be measured with a fairly high degree of precision. Since the signal coming from single emitters is extremely weak, the uncertainties are more critical. It is expected, however, that $\sigma_{2p} \approx 500 - 5000$ GM, depending on the particle's size.

3.5.3 Raster scan

The raster scan is performed after the SH signal is optimized by fine tuning the particle's position as well the wavelength. The image is formed by scanning the sample following a sawtooth wave across a small area (about 9–16 μm^2) in 50 nm increments.

The first tests used an over-concentrated solution, without ultrasonic bath and two depositions, so that the particles are close together and form clusters. The result is shown in Figures 31(a)–31(b). One sees several peaks but no clear definition from a single emitter. This kind of deposition may be suitable for applications when labeling a large area is more important than single point resolution. Figures 31(c)–31(d) show a more disperse deposition and single emitters are now clearly seen.

Those pictures were made without spatial filters (pinhole), so they represent a PSF for a conventional microscope, but operating in SH imaging mode. As discussed previously, the parametric process by itself is enough to increase the intrinsic resolution. Finally, Figures 31(e)–31(f) show single emitters recorded after the signal passes through the 10

Figure 31 – Raster scan images. (a)–(b) Concentrated deposition; (c)–(d) Single emitters recorded without using a spatial filter; (e)–(f) Confocal microscopy (10 μm pinhole).

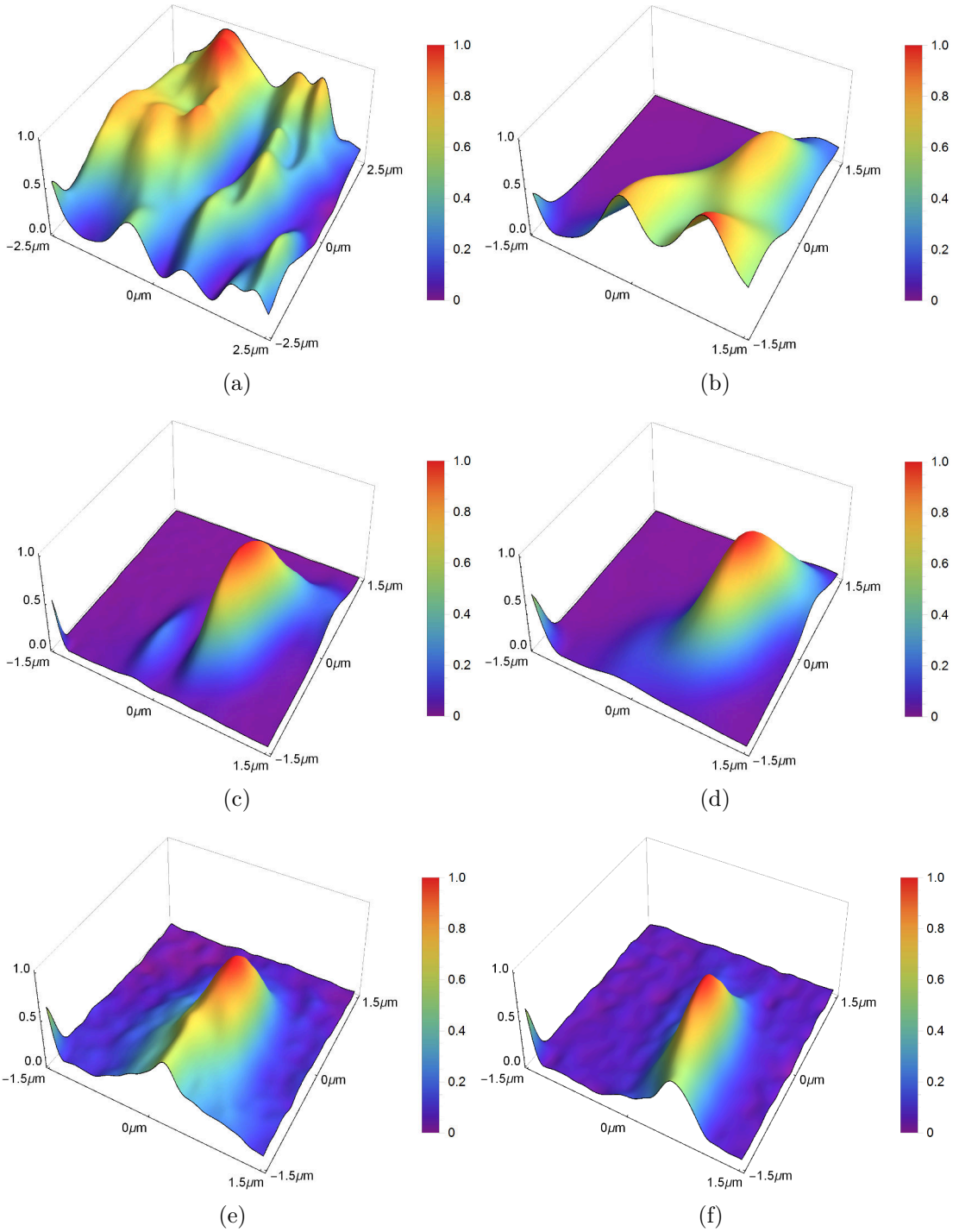

μm pinhole. Those pictures represent the radial PSF and show a good agreement with Equation 2.46.

A full 3D raster scan for a single emitter is represented in Figure 32. That kind of measurement represents one of the most notorious qualities of a CSOMs: the ability to reconstruct a 3D object with high resolution by stacking confocal image slices at z

intervals. For objects much bigger than the PSF, this technique is a viable alternative to fluorescence microscopy for biological applications.

Figure 32 – 3D raster scan. The dotted cube represents an area taken away from the 3D raster scan, so the inside of the PSF can be seen, since it is a 4D object.

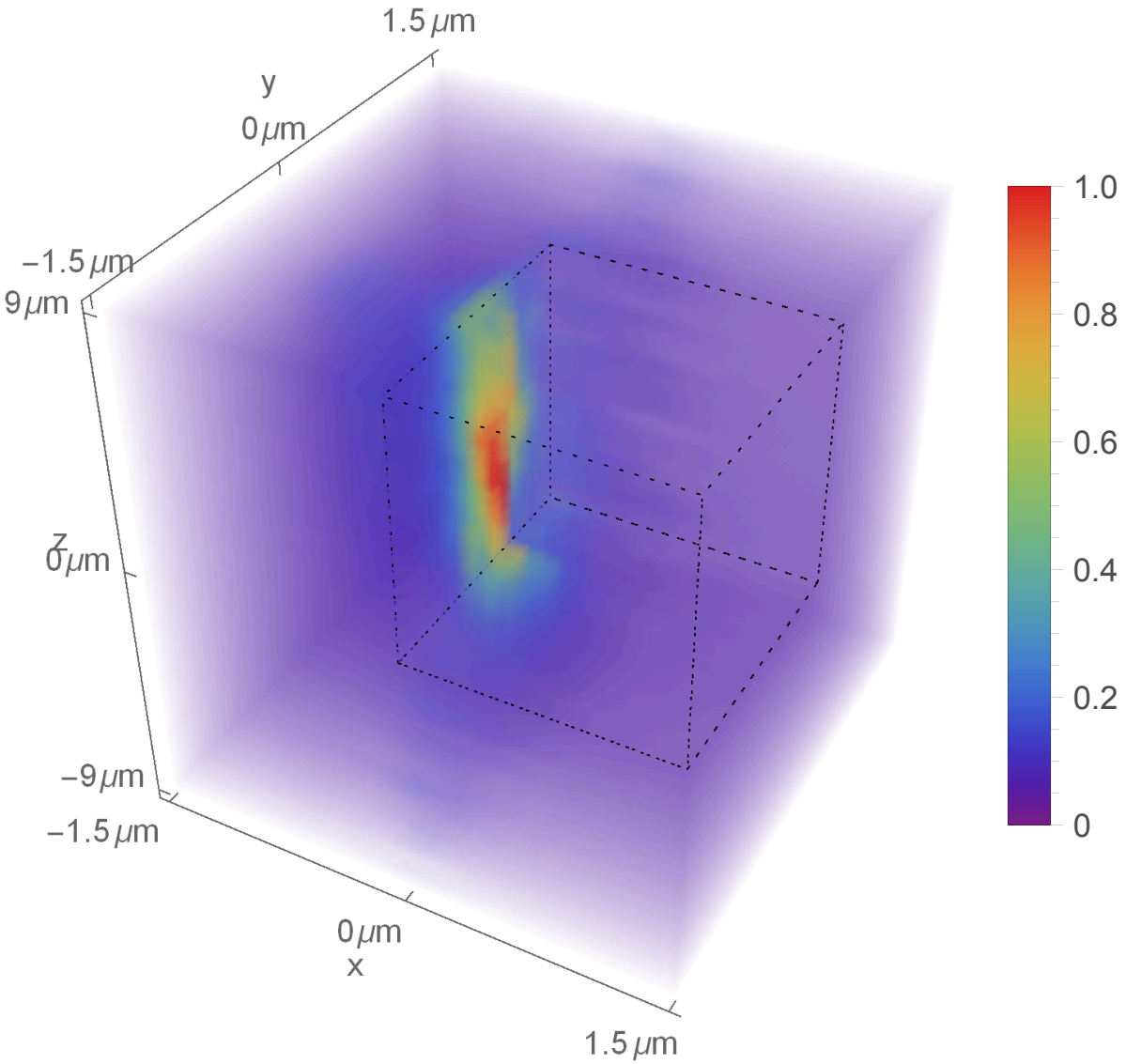

3.6 Higher harmonics confocal microscopy

As mentioned in the previous sections, the experimental routine was focused in the SHG due to several technical limitations. However, similar BBO particles are known to generate up to the 5th-order harmonics under excitation at 2 μm, 100 fs pulses, repetition rate of 1 kHz and average power of 25–45 mW (MIRANDA, 2016). That experiment uses more favorable excitation and collection conditions as well a much larger number of particles. For comparison, in (MIRANDA, 2016), the peak power in the focal spot is

$\approx 5 \times 10^8$ W, for a focal spot diameter of ≈ 30 μm containing $\approx 10^{10}$ NCs against the $\approx 3 \times 10^4$ W for our experiment with single NCs. Therefore, comparing those distinct experimental conditions, a factor of $F \propto 10^{10} \times (10^4)^2 \approx 10^{18}$ had to be overcome.

As a result of the technical limitations, only the THG spectra were recorded and even so the results have a poor S/N ratio, therefore, no further imaging analysis was possible. The TH signal was recorded by optimizing the SH detection and then shifting the monochromator to the expected spectral range. The integration time had to be raised for a second/step and special care had to be taken for any spurious light. Unfortunately, the poor S/N ratio does not allow the power dependency to be taken. The spectral position and the fact that the signal disappeared when the particle was moved away from the focal position strongly suggests that the peak in Figure 33 is indeed the TH signal coming from a single BBO NCs. Equation 3.6 gives a narrowing factor of ≈ 0.19 for the TH so the spectral width would be limited by the monochromator resolution.

Figure 33 – THG spectrum. The peak position is ≈ 272.5 nm. The signal is too weak for a FWHM to be determined as well the power dependency.

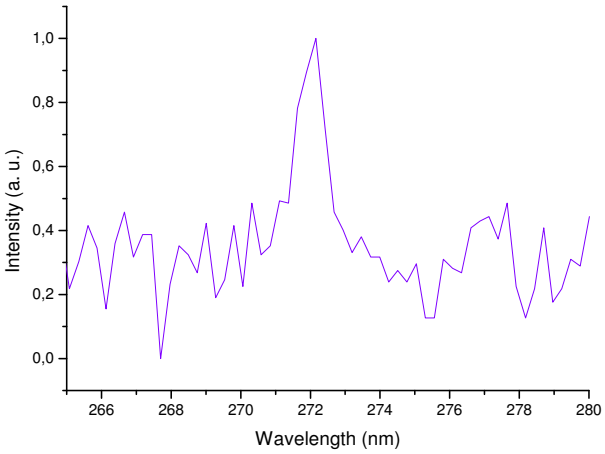

The TH is useful for confocal microscopy because in principle it is present for all nonlinear emitters and do not depend on the existence of inversion symmetry. Since the confocal microscope is homemade, it has the capability of several improvements depending on the kind of experiment to be carried on. For instance, the APD route can be useful for fluorescence measurements in the visible range and a collection setup by transmission can be added specially for the THG.

4 CONCLUSIONS AND PERSPECTIVES

In this M. Sc. thesis, it was shown a study of nonlinear imaging of single β–BBO nanocrystals. From the sample's basic characterization, one can see the apparent polycrystalline structure of the nanoneedles, although our technique is effectively insensitive to the presence of those defects. This is important because a multiple domain nanocrystal would jeopardize the polarization resolved microscopy, since the polarization patterns would overlap. The individual nanocrystals exhibited second and third harmonic generation, but only the second harmonic had enough intensity to be characterized and studied properly. For the second harmonic, the spectral behavior matched the expectations for the infrared pump and the two-photons parametric process. The polarization response of the second harmonic also allowed to determine the individual crystals' orientation following a model derived from the β–BBO group symmetries.

Some of the causes of the poor third harmonic detection can be overcome by changing the experimental setup to a transmission geometry, so an ideal optics for the excitation can be combined with more suited optics for collecting the signal at a deeper ultraviolet region. Another option reported in the literature is the use of a smaller numerical aperture objective for excitation and a higher numerical aperture one for collection, so a larger excitation spot is produced, thus allowing images to be taken without scanning, which is much faster. The gain in acquisition speed can be invested in integration time, so even weaker signals can be detected. Moreover, the transmission setup makes modeling of the excitation behavior much simpler by avoiding a tightly focused beam regime that adds complex polarization components (KIM et al., 2013; TIMOFEEVA et al., 2016). Another option to generate different wavelengths is to use a sum of frequencies, for it is still a second-order process so it is expected to occur with greater efficiency than higher order harmonics in single emitters. A longer excitation wavelength can also be used to bring the nonlinear signals to the visible range, where the APD is more sensitive. Since the homemade microscope is quite versatile, it is relatively easy to adapt the optics for other experiments and particles.

According to the imaging theory for confocal microscopy, the third harmonic promotes a significant improvement in resolution, even without any spatial filtering, so it is of great interest for biological applications. The gain in resolution for the second harmonic however is still considerable, as shown by the experimental results of this work. Therefore, stable single emitters free of bleaching and blinking can be developed for high resolution microscopy as well as their nonlinear properties at the nanoscale can be quantified.

BIBLIOGRAPHY

ADUR, J. et al. Second harmonic generation microscopy as a powerful diagnostic imaging modality for human ovarian cancer. *Journal of Biophotonics*, v. 7, n. 1-2, p. 37–48, 2014.

BACHE, M. et al. The anisotropic Kerr nonlinear refractive index of the beta-barium borate (β-BaB_2O_4) nonlinear crystal. *Opt. Mater. Express*, v. 3, n. 3, p. 357–382, 2013.

BELLINI, M. et al. Domain-engineered ferroelectric crystals for nonlinear and quantum optics. In: *Ferroelectric Crystals for Photonic Applications: Including Nanoscale Fabrication and Characterization Techniques*. Berlin, Heidelberg: Springer Berlin Heidelberg, 2014. p. 285–311.

BIJEESH, M. M. et al. Confocal imaging of single $BaTiO_3$ nanoparticles by two-photon photothermal microscopy. *Nature Scientific Reports*, v. 7, n. 1643, p. 1–9, 2017.

BOYD, R. W. Chapter 1 - The Nonlinear Optical Susceptibility. In: *Nonlinear Optics*. Third edition. Burlington: Academic Press, 2008. p. 1–67.

CHAN, S. et al. Second harmonic generation in zinc oxide nanorods. *Applied Physics B*, v. 84, n. 1, p. 351–355, 2006.

CORLE, T. R.; KINO, G. S. CHAPTER 1 - Introduction. In: _____. *Confocal Scanning Optical Microscopy and Related Imaging Systems*. Burlington: Academic Press, 1996. p. 1–66.

CORLE, T. R.; KINO, G. S. CHAPTER 2 - Instruments. In: _____. *Confocal Scanning Optical Microscopy and Related Imaging Systems*. Burlington: Academic Press, 1996. p. 67–145.

CORLE, T. R.; KINO, G. S. CHAPTER 3 - Depth and Transverse Resolution. In: _____. *Confocal Scanning Optical Microscopy and Related Imaging Systems*. Burlington: Academic Press, 1996. p. 147–223.

DANTEC, R. L. et al. Ensemble and Individual Characterization of the Nonlinear Optical Properties of ZnO and $BaTiO_3$ Nanocrystals. *The Journal of Physical Chemistry C*, v. 115, n. 31, p. 15140–15146, 2011.

DENEV, S. A. et al. Probing ferroelectrics using optical second harmonic generation. *Journal of the American Ceramic Society*, v. 94, n. 9, p. 2699–2727, 2011.

DEYRA, L. et al. Impact of BaB_2O_4 growth method on frequency conversion to the deep ultra-violet. *Solid State Sciences*, v. 50, p. 97–100, 2015.

DOW, X. Y. et al. Second-harmonic generation correlation spectroscopy for characterizing translational diffusing motion of protein nanocrystals. Supporting information. *Acta Cryst.*, v. 72, p. sup–1–5, 2016.

DUTTO, F. et al. Nonlinear Optical Response in Single Alkaline Niobate Nanowires. *Nano Letters*, v. 10, n. 6, p. 2517–2521, 2011.

ECKARDT, R. C.; BYER, R. L. Measurement of nonlinear optical coefficients by phase-matched harmonic generation. *Proc. SPIE*, v. 1561, p. 119–127, 1991.

EHMKE, T. et al. Spectral behavior of second harmonic signals from organic and non-organic materials in multiphoton microscopy. *AIP Advances*, v. 8, n. 5, p. 084903–1–6, 2015.

FRANKEN, P. A. et al. Generation of optical harmonics. *Phys. Rev. Lett.*, v. 7, p. 118–119, 1961.

GEREN, K. et al. Second-order susceptibilities of ZnO nanorods from forward second-harmonic scattering. *Journal of Applied Physics*, v. 105, n. 6, p. 063531–1–5, 2009.

GRANGE, R. et al. Lithium niobate nanowires synthesis, optical properties, and manipulation. *Applied Physics Letters*, v. 95, n. 14, p. 143105–1–3, 2009.

HAHN, T. *International Tables for Crystallography Volume A: Space-group symmetry*. Fifth edition. [S.l.]: Springer Netherlands, 2005. (International Tables for Crystallography A).

HOOVER, E. E.; SQUIER, J. A. Advances in multiphoton microscopy technology. *Nat Photon*, v. 7, n. 2, p. 93–101, 2013.

HSIEH, C.-L. et al. Three-dimensional harmonic holographic microcopy using nanoparticles as probes for cell imaging. *Opt. Express*, v. 17, n. 4, p. 2880–2891, 2009.

HSIEH, C.-L. et al. Three-dimensional harmonic holographic microcopy using nanoparticles as probes for cell imaging: erratum. *Opt. Express*, v. 18, n. 4, p. 3456–3457, 2010.

HSIEH, C.-L. et al. Second harmonic generation from nanocrystals under linearly and circularly polarized excitations. *Opt. Express*, v. 18, n. 11, p. 11917–11932, 2010.

KADOUCH, D. et al. Diagnostic accuracy of confocal microscopy imaging versus punch biopsy for diagnosing and subtyping basal cell carcinoma. *Journal of the European Academy of Dermatology and Venereology*, p. 1–21, 2017.

KIM, E. et al. Second-Harmonic Generation of Single $BaTiO_3$ Nanoparticles down to 22 nm Diameter. *ACS Nano*, v. 7, n. 6, p. 5343–5349, 2013.

KITTEL, C. *Introduction to Solid State Physics*. 6th edition. ed. New York: John Wiley & Sons, Inc., 1986.

KYMIONIS, G. D. et al. Correlation of the Corneal Collagen Cross-Linking Demarcation Line Using Confocal Microscopy and Anterior Segment Optical Coherence Tomography in Keratoconic Patients. *American Journal of Ophthalmology*, v. 157, n. 1, p. 110–115.e1, 2014.

LIU, J. et al. Second Harmonic Super-resolution Microscopy for Quantification of mRNA at Single Copy Sensitivity. *ACS Nano*, v. 8, n. 12, p. 12418–12427, 2014.

LIU, J. et al. Single-cell screening and quantification of transcripts in cancer tissues by second-harmonic generation microscopy. *Journal of Biomedical Optics*, v. 20, n. 9, p. 096016–1–7, 2015.

LOC, L. X. et al. Photostable second-harmonic generation from a single $KTiOPO_4$ nanocrystal for nonlinear microscopy. *Small*, v. 4, n. 9, p. 1332–1336, 2008.

MAYER, L. et al. Dual light-emitting nanoparticles: second harmonic generation combined with rare-earth photoluminescence. *J. Mater. Chem. C*, v. 2, p. 7681–7686, 2014.

MAZUMDER, N. et al. Polarization resolved second harmonic microscopy. *Methods*, xxx, n. xxx, p. 1–14, 2017.

MIRANDA, I. P. de. *Espalhamento hiper-Rayleigh de alta ordem em nanocristais de BBO. Master's thesis*. Recife: Universidade Federal de Pernambuco, 2016.

NAKAYAMA, Y. et al. Tunable nanowire nonlinear optical probe. *Nature*, v. 447, p. 1098–1101, 2007.

NEWNHAM, R. E. Chapter 5 - Tensors and physical properties. In: *Properties of Materials Anisotropy, Symmetry, Structure*. New York: Oxford University Press, 2005. p. 30–34.

NOVOTNY, L.; HECHT, B. Propagation and focusing of optical fields. In: *Principles of Nano-Optics*. United Kingdom: Cambridge University Press, 2012. p. 45–85.

NYE, J. F. *Physical Properties of Crystals. Their Representation by Tensors and Matrices*. Great Britain: Oxford University Press, 1985.

POWERS, P. E.; HAUS, J. W. *Fundamentals of Nonlinear Optics*. Second edition. Boca Raton, FL: CRC Press, 2017.

PU, Y.; PSALTIS, D. Second-harmonic radiating imaging probes and harmonic holography. *Proc. SPIE*, v. 9956, p. 995608–1–13, 2016.

RAJADHYAKSHA, M. et al. Reflectance confocal microscopy of skin in vivo: From bench to bedside. *Lasers in Surgery and Medicine*, v. 49, n. 1, p. 7–19, 2017.

RICHARDS, B.; WOLF, E. Electromagnetic Diffraction in Optical Systems. II. Structure of the Image Field in an Aplanatic System. *Proceedings of the Royal Society of London A: Mathematical, Physical and Engineering Sciences*, v. 253, n. 1274, p. 358–379, 1959.

RODRIGUEZ, E. V. et al. Hyper-Rayleigh scattering from $BaTiO_3$ and $PbTiO_3$ nanocrystals. *Chemical Physics Letters*, v. 467, n. 4, p. 335–338, 2009.

SÁNCHEZ, E. D. C. *Optically detected magnetic resonance in nanodiamonds with single nitrogen–vacancy defects. Master's Thesis*. Recife: Universidade Federal de Pernambuco, 2016.

SANDISON, D. R. et al. Quantitative comparison of background rejection, signal-to-noise ratio, and resolution in confocal and full-field laser scanning microscopes. *Appl. Opt.*, v. 34, n. 19, p. 3576–3588, 1995.

SCHMIDT, C. et al. Multi-Order Investigation of the Nonlinear Susceptibility Tensors of Individual Nanoparticles. *Nature Scientific Reports*, v. 6, p. 1–9, 2016.

TANG, Z.; XING, D.; LIU, S. Imaging theory of nonlinear second harmonic and third harmonic generations in confocal microscopy. *Science in China Series G: Physics, Mechanics and Astronomy*, v. 47, n. 1, p. 8–16, 2004.

THEODOSSIOU, T. A. et al. Second harmonic generation confocal microscopy of collagen type i from rat tendon cryosections. *Biophysical Journal*, v. 91, n. 12, p. 4665–4677, 2006.

TIMOFEEVA, M. et al. Polar Second-Harmonic Imaging to Resolve Pure and Mixed Crystal Phases along GaAs Nanowires. *Nano Letters*, v. 16, n. 10, p. 6290–6297, 2016.

URBAN, B. E. et al. Optimization of nonlinear optical properties of ZnO micro and nanocrystals for biophotonics. *Opt. Mater. Express*, v. 1, n. 4, p. 658–669, 2011.

VILLANI, E. et al. In Vivo Confocal Microscopy of the Ocular Surface: From Bench to Bedside. *Current Eye Research*, v. 39, n. 3, p. 213–231, 2014.

WANG, Y. et al. Synthesis and second harmonic generation response of $KNbO_3$ nanoneedles. *Journal of Crystal Growth*, v. 341, n. 1, p. 42–45, 2012.

WEIGELIN, B.; BAKKER, G.-J.; FRIEDL, P. Third harmonic generation microscopy of cells and tissue organization. *Journal of Cell Science*, v. 129, n. 2, p. 245–255, 2016.

WILSON, T. Optical sectioning in confocal fluorescent microscopes. *Journal of Microscopy*, v. 154, n. 2, p. 143–156, 1989.

WILSON, T. Resolution and optical sectioning in the confocal microscope. *Journal of Microscopy*, Blackwell Publishing Ltd, v. 244, n. 2, p. 113–121, 2011.

WILSON, T.; CARLINI, A. R. Size of the detector in confocal imaging systems. *Opt. Lett.*, v. 12, n. 4, p. 227–229, 1987.

WILSON, T.; CARLINI, A. R. Three-dimensional imaging in confocal imaging systems with finite sized detectors. *Journal of Microscopy*, v. 149, n. 1, p. 51–66, 1988.

WNUK, P. et al. Coherent nonlinear emission from a single KTP nanoparticle with broadband femtosecond pulses. *Opt. Express*, v. 17, n. 6, p. 4652–4658, 2009.

WOLF, J.-P. Ultrafast nano-biophotonics. In: *Nano-Optics: Principles Enabling Basic Research and Applications*. Dordrecht: Springer Netherlands, 2017. p. 191–212.

XIAO, Q. et al. Morphology and polarization-dependent second harmonic generation in single hexagonal sodium niobate micro/nano-crystals. *J. Mater. Chem. C*, v. 3, n. 16, p. 4070–4076, 2015.

YARIV, A. Chapter 16 - Introduction to Nonlinear Optics–Second-Harmonic Generation. In: *Quantum Electronics*. Third edition. New York: John Willey & Sons, 1989. p. 378–406.

ZERNIKE, F.; MIDWINTER, J. Chapter 2 - Nonlinear Optics. In: *Applied Nonlinear Optics*. New York: John Willey & Sons, 1973. p. 25–53.

ZUGEL, S. A.; LYTLE, F. E. Comparison of 90° and Epi-Geometry for Two-Photon Excitation in Capillaries. *Applied Spectroscopy*, v. 54, n. 10, p. 1490–1494, 2000.

APPENDIX A – POSTER PRESENTED AT 10TH INTERNATIONAL CONFERENCE ON NANOPHOTONICS (ICNP) 2017 (HONORABLE MENTION).

Second-harmonic imaging microscopy of single β-BBO nanocrystals

Rodrigo G. dos Santos[1], Lauro J. Q. Maia[2], Cid B. de Araújo[1], Leonardo de S. Menezes[1]

[1]Departamento de Física, Universidade Federal de Pernambuco, Recife – PE
[2]Instituto de Física, Universidade Federal de Goiás, Goiânia - GO

ICNP 2017 | 10th International Conference on Nanophotonics
July 02-05, 2017 | Recife-PE - Brazil

Motivation

- Confocal Microscopy for studying single β-Barium Borate (BBO) nanocrystals (NCs).
- Raster scan and polarization resolved microscopy for the single emitters by second harmonic generation (SHG).

Confocal microscopy

- Simplifyied diagram of a confocal microscope for studying single nanoparticles

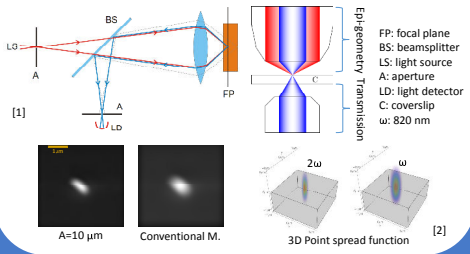

The sample – basic characterization

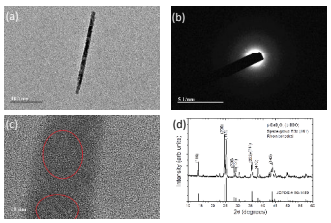

(a) TEM; (b) SAED; (c) HR–TEM; (d) XRD

Experimental setup

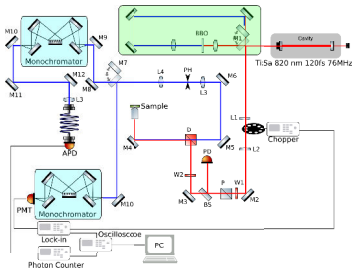

M1-M3: dielectric mirrors; M4-M12: metallic mirrors; L1-L4: convex lenses; BS: beamsplitter; W1-W2: half-wave plates; P: polarizer; D: dichroic mirror; PD: fotodetector.

Detection of single nanocrystals

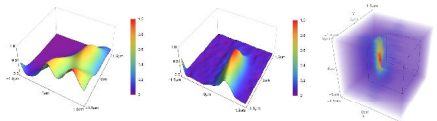

3 NCs (Conventional M.) 1 NC (Confocal M.) 3D PSF

Polarization response

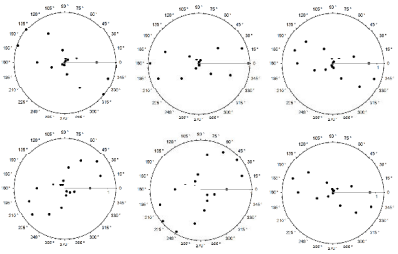

[3,4]

Spectral data

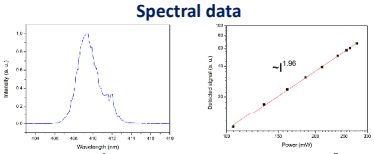

$\Delta\lambda_n = \frac{1}{n\sqrt{n}}\Delta\lambda_f$ $I^{(2\omega)} \propto \left(I^{(\omega)}\right)^2$

Perspectives

- Higher harmonics imaging microscopy by transmission geometry and/or excitation in longer wavelengths.
- Determination of the $\chi^{(2)}$ components for single BBO NCs.
- Improvement of data acquisition speed and detection sensitivity.

References

[1] T. R. Corle and G. S. Kino, *Confocal Scanning Optical Microscopy and Related Systems*, Academic Press, Burlington (1996).
[2] T. Wilson and A. R. Carlini, J. Microsc. **149**, 51–66 (1988).
[3] C.-L. Hsieh, Y. Pu, R. Grange, and D. Psaltis, Opt. Express **18**, 11917–11932 (2010).
[4] C. Schmidt *et al*, Sci. Rep. **6**, 25415 (2016).

Acknowledgements

- CAPES
- CNPq: Photonics National Institute - INFo
- FACEPE: PRONEX Project
- RGS acknowledges CNPQ master's fellowship